A Portal Imager-Based Patient Dosimetry System

by

James M. D. Roberts
B.Sc., St. Francis Xavier University, 2011

A Thesis Submitted in Partial Fulfillment of the
Requirements for the Degree of

MASTER OF SCIENCE

in the Department of Physics and Astronomy

University of Victoria

A Portal Imager-Based Patient Dosimetry System

by

James M. D. Roberts
B.Sc., St. Francis Xavier University, 2011

Supervisory Committee

Dr. W. Ansbacher, Co-supervisor
(Department of Physics and Astronomy, BC Cancer Agency - Vancouver Island Centre)

Dr. A. Jirasek, Co-supervisor
(Department of Physics and Astronomy)

Dr. P. Basran, Departmental Member
(Department of Physics and Astronomy, BC Cancer Agency - Vancouver Island Centre)

Supervisory Committee

Dr. W. Ansbacher, Co-supervisor
(Department of Physics and Astronomy, BC Cancer Agency - Vancouver Island Centre)

Dr. A. Jirasek, Co-supervisor
(Department of Physics and Astronomy)

Dr. P. Basran, Departmental Member
(Department of Physics and Astronomy, BC Cancer Agency - Vancouver Island Centre)

ABSTRACT

A technique for the *in vivo* dose verification of intensity modulated radiation therapy (IMRT) has been developed. An electronic portal image, calibrated in terms of absolute dose, is acquired for each radiation field following transmission through the patient at the time of treatment. For an IMRT field, the portal image signal is back-projected through a model of the patient in order to calculate the dose at the isocentric plane perpendicular to the beam central axis.

The IMRT *in vivo* dose verification technique was adapted for volumetric modulated arc therapy (VMAT) treatments when a single dosimetric image is acquired over an arc. The patient dose along axis of gantry rotation can be directly related to the signal along the vertical axis of EPIs in integrated mode. In this novel VMAT *in vivo* dosimetry technique, the portal image signal is back-projected through a rotationally averaged model of the patient to calculate a 1D *in vivo* dose along the axis of gantry rotation.

A research ethics board clinical study was approved and transmission portal images were acquired at regular intervals from human subjects. Portal image-derived isocenter point doses were in good agreement with treatment planning system (TPS) calculations for IMRT (mean difference $\overline{\delta_{PI}} = 0.0\%$, standard deviation of the differences $\sigma_{\delta_{PI}} = 4.3\%$) and VMAT ($\overline{\delta_{PI}} = 1.1\%$, $\sigma_{\delta_{PI}} = 1.7\%$). The one-dimensional (VMAT) and two-dimensional (IMRT) reconstructed doses were further analyzed by calculating mean dose differences and $\gamma-$evaluation pass-rates, which were also shown to be in good agreement with TPS calculations.

The portal image-based *in vivo* dosimetry techniques were shown to be clinically feasible, with reconstruction times on the order of minutes for the first fraction and less than one minute for each fraction thereafter.

Contents

List of Tables

List of Figures

ACKNOWLEDGEMENTS

I wish to express my sincere gratitude to my supervisors, Dr. Will Ansbacher and Dr. Andrew Jirasek, for their support and mentorship throughout my studies. In addition, I wish to thank Dr. Parminder Basran for many useful discussions, and the Radiation Therapy Program at the BC Cancer Agency - Vancouver Island Centre—in particular Nancy Saunders, Jim Runkel, Kelly Earnshaw and Debra Campbell—for facilitating and assisting with the clinical research undertaken in this work. Finally, I would like to thank the faculty, staff and students at the University of Victoria and the BCCA-VIC who have helped make my time here so memorable.

Chapter 1

Introduction

1.1 Radiation therapy

1.1.1 Introduction to radiation therapy

Radiation therapy involves using the interactions of ionizing radiation with matter to treat certain malignancies and benign conditions. More than half of all patients at the BC Cancer Agency (approximately 55%) will receive radiation therapy at some point during their care [1]. Radiation therapy is prescribed either as part of a curative treatment plan or as part of a symptom relief regimen.

The most common types of ionizing radiation used for radiation therapy are high energy photons (X-rays and γ-rays) and electrons. Ionizing radiation can directly or indirectly damage deoxyribonucleic acid (DNA) in cells. Direct damage is caused when the radiation ionizes DNA strands, whereas indirect damage occurs through free radical production and reaction with DNA following the radiolysis of water. The integrity of DNA is essential for cellular proliferation. DNA damage can lead to cellular death primarily by apoptosis, though it should be noted that a number of other mechanisms may be involved in cellular death.

When radiation therapy is indicated for a patient, the patient first receives a planning X-ray computed tomography (CT) scan. The radiation oncologist contours the tumour volume and critical organs on the CT scan and prescribes the radiation dose. A radiation dosimetrist plans and optimizes the patient's unique treatment based on standardized protocols and the oncologist's instructions. The physics staff verifies that the plan satisfies quality assurance protocols. The course of treatment is typically delivered over a number of weeks; each treatment session is known as a "fraction". For example, in prostate cancer treatment, a 74 Gy dose might be prescribed to the prostate, delivered over thirty seven daily 2 Gy fractions.

High energy photons and electrons are produced in dedicated treatment rooms by clinical linear accelerators. The linear accelerator gantry is able to rotate about a fixed point known as the isocenter, which is often chosen to be at the centre of the tumour. The ability of the linear accelerator to rotate about the patient allows for treatment beams to enter from multiple directions, allowing doses to converge at or near the isocentre while minimizing dose to healthy (non-malignant) tissue.

Healthy tissues can be spared by modulating the radiation beam. A device known as a multi-leaf collimator (MLC) allows for the radiation field to be shaped precisely to the contours of the tumour. The MLC also controls the intensity of the beam by blocking given areas of the field for set periods of time while leaving other areas open; it is a dynamic beam shaping device. Static-field intensity modulated radiation therapy (referred to as IMRT) and volumetric-modulated arc therapy (VMAT) are two of the most advanced radiation delivery techniques and make extensive use of the MLC. Both techniques have allowed for radiation dose to malignant tissues to escalate while reducing the radiation exposure to healthy tissues [2–4].

IMRT is one of the most frequently employed modern techniques for shaping radiation fields in order to deliver a maximum radiation dose to malignant tissues while sparing normal tissue and critical organs. The shapes and intensities of multiple radiation fields are optimized at fixed angles relative to the linear accelerator using fluence-based optimization algorithms. Typically, five to seven treatment beams are used per plan in order to achieve uniform coverage of the target volume(s) while sparing a maximum amount of healthy tissue.

In VMAT, the angles of the beams are not fixed during radiation delivery; rather, the radiation dose is delivered in a continuous arc around the patient as the gantry rotates. The planning for this radiation therapy technique is based on a direct-aperture optimization of the radiation fields and employs similar beam-shaping methods as IMRT. VMAT retains the clinical advantages of IMRT while generally requiring less treatment time to deliver the same radiation dose distribution [5–8].

In Figure 1.1, example prostate cancer treatment dose calculations using IMRT and VMAT are shown. The same prescription and optimization objectives were used to plan the treatment. The inherent nature of each technique is demonstrated: IMRT uses a fixed number of beams (the entrances and exits of which are clear), whereas VMAT uses a continuous beam delivery over an arc. In both plans, the same treatment objectives were met.

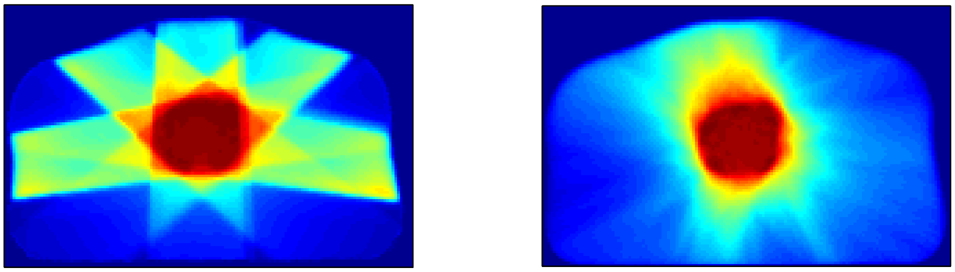

Figure 1.1: Five-field IMRT prostate planned dose (axial plane), on left; the same patient but replanned using two VMAT arcs, on right. Red denotes high dose regions; blue denotes low dose regions.

1.1.2 Electronic portal imaging devices

The accuracy of radiation therapy relies largely on the patient being set up on the day of treatment in the same position their radiation therapy was planned. To that end, patients are tattooed or marked in order to establish a patient coordinate system that can be reproduced at the time of treatment. Accurate lasers are used to align the tattoos so that the reference position from the X-ray CT scan matches the treatment position.

Acquiring portal images (i.e. those images taken using the treatment radiation beam after it has exited the patient) has become an effective method to confirm accurate beam placement and patient setup [9]. The first portal images were acquired using radiographic film; however, recent advances in technology have allowed for the digital acquisition of these images using electronic portal imaging devices (EPIDs).

EPIDs are two-dimensional radiation detectors that are positioned directly across from the X-ray source of a linear accelerator. In their most basic form, these devices are capable of detecting the intensity of the exit radiation beam in a plane. The intensity variations in the portal image signal are the result of differences in anatomical structures (ie. bone, lung, and soft tissue) and of the planned beam modulation that is a key feature of IMRT and VMAT. In Figure 1.2, a clinical linear accelerator is shown together with an electronic portal imaging device across from the linear accelerator gantry, beneath the treatment couch. The kilovoltage (kV) X-ray imager is also shown in a partially retracted position.

Patient positioning verification using portal images has been well documented [10, 11]. Typically, bony anatomy from a short exposure is matched against the corresponding anatomy on planning digitally reconstructed radiographs (DRRs) to

Figure 1.2: Varian TrueBeam (Varian Medical Systems, Palo Alto CA) linear accelerator with EPID deployed beneath the treatment bed. The patient most often lies in the supine position, head first on the treatment bed.

determine appropriate positional adjustments before treatment if the initial setup is outside of institutional tolerance values. Orthogonal set-up electronic portal images are routinely obtained at the BC Cancer Agency - Vancouver Island Centre (BCCA-VIC) in order to monitor patient alignment throughout a course of treatment.

In addition to the radiographic function of EPIDs, the response of these devices to ionizing radiation has been investigated for applications to dosimetry and treatment verification [12]. When operated in “integrated” (or “dosimetry”) mode, two-dimensional information about each complete treatment radiation beam can be captured in the beam’s eye view throughout the treatment session. Van Elmpt et al. published a comprehensive systematic review of EPID dosimetry in 2008 [13]; they describe broadly two common classes of EPID dosimetry. The first, “non-transmission” involves delivering the planned radiation in the absence of the patient and recording the signal on the EPID. The second, “transmission” involves recording the signal on the EPID following transmission through a patient (or phantom in the case of pre-treatment verification). This second class of EPID dosimetry is also commonly termed “transit” dosimetry, and when used to measure patient dose it can fall under the much broader class of “*in vivo*” dosimetry.

1.2 Motivation for *in vivo* dosimetry

The current IMRT pre-treatment patient specific quality assurance (QA) procedure at the BCCA-VIC is EPID non-transmission verification [14]. Portal images are obtained for each radiation beam in the absence of the patient before the first treatment. The resulting images are then used to reconstruct a three-dimensional dose distribution in a virtual cylinder that can be compared to the planned dose. This procedure has been recently adapted to perform three-dimensional pre-treatment dose reconstruction using cine-mode (continuous) imaging for VMAT treatments [15].

These pre-treatment quality assurance procedures ensure that the treatment can be delivered as planned, but do not take into account patient- and machine-specific uncertainties that can vary between treatments. Patient-specific uncertainties can include involuntary movements or shifts, organ motion, weight loss or gain, and unplanned air cavities (e.g. rectal gas pockets in prostate radiotherapy). Machine-specific uncertainties can include output variations, collimation and modulation errors, and monitor unit (user-defined machine output) errors.

The inevitability of uncertainties in radiation therapy - as well as recent (although rare) accidents in radiation therapy [16, 17] - have prompted the investigation of various dosimeters for routine patient dose monitoring (so-called "*in vivo*" dosimetry) over a course of treatment. Individual patient dose monitoring is gradually becoming the standard of care, particularly in Europe where countries such as France and Sweden require *in vivo* radiation therapy dose verification [18, 19].

Several European institutions have used thermoluminescent detectors (TLDs) and metal oxide semiconductor field effect transistor (MOSFET) dosimeters for intracavitary dose measurements [20]. However, such dose measurements can be uncomfortable to the patient and can require a significant time investment to process. At the BCCA-VIC, patient-level dose monitoring is currently restricted to TLD point dose measurements in limited circumstances.

1.3 *In vivo* EPID dosimetry

In *in vivo* EPID dosimetry, portal images are acquired for each treatment beam following transmission of the beam through the patient. By using a knowledge of the patient setup, based on the patient CT data set, the exit radiation fluence recorded by the EPID is back-projected and used to calculate the dose to the patient. Portal images have the advantage of being able to provide high resolution two-dimensional dose planes, unlike conventional *in vivo* point-dose dosimeters.

It has been contended that *in vivo* dosimetry is often "expensive and unnecessary," as reviewed by Leman [21]. Given the generally established safety of modern radiation therapy, some have questioned the need to implement *in vivo* dosimetry programs. However, electronic portal imaging devices are now standard components of many clinical linear accelerators. Compared to diode *in vivo* dosimetry, for example, no additional components or devices are required. Furthermore, the EPID set-up, image acquisition, and image processing times are minimal.

In order to perform transit EPID dosimetry, it is necessary to construct an accurate model of all the materials in the beam's path above the EPID. Any discrepancies between the planning CT setup (i.e. patient support structures) and treatment setup should be resolved before attempting to reconstruct dose.

Portal image-based *in vivo* dosimetry techniques have been developed and refined by several institutions - as early as 1996 for three-dimensional conformal radiation therapy (3DCRT) [22]. More recently, a group at the Netherlands Cancer Institute Antoni van Leeuwenhoek Hospital (NKI-AVL) has developed an established portal image back projection technique for IMRT treatments [23] and VMAT treatments [24].

1.4 Thesis scope

This thesis presents the development and characterization of an IMRT *in vivo* EPID dosimetry technique. The EPID was calibrated in terms of absolute dose, and the dose plane recorded by the EPID was back-projected through a model of the patient to calculate the isocentric dose plane in the patient for each IMRT beam.

In addition, a novel one-dimensional *in vivo* dose reconstruction technique for VMAT treatments was developed by adapting the IMRT dose back-projection model. The proposed technique solves the problem of relating single integrated portal images to an *in vivo* dose when continuous imaging is not available [24]. The approach taken is to treat the continuous arc as a single static field incident upon a rotationally averaged representation of the patient. The two-dimensional dose back-projection technique is then performed in this collapsed geometry, and the central profile (dose along the axis of gantry rotation) is examined. The dose along the axis of gantry rotation in the new geometry is equal to the dose along the true axis of gantry rotation in the patient.

An ethics review board approved protocol was established and transit portal images were acquired from ten human participants undergoing IMRT and three human participants undergoing VMAT at the BCCA-VIC. The purpose of this study was to validate the transit dosimetry models developed for the two techniques (IMRT and VMAT).

The organization of this thesis is as follows:

Chapter 2 discusses the physics of radiation therapy, the dosimetric characteristics of EPIDs, and a brief literature review of *in vivo* EPID dosimetry techniques for IMRT and VMAT.

Chapter 3 outlines the experiments that were performed in order to characterize the EPID used in this study and to develop the back-projection model.

Chapter 4 presents the results of the initial EPID characterizations and relevant back-projection model parameters.

Chapter 5 presents the results of a clinical study to validate the IMRT and VMAT back-projection models.

Chapter 6 contains an analysis of the results of this study; in particular, as the results pertain to the clinical validation of the back-projection models.

Chapter 7 concludes the thesis. Presented in this chapter is an overview of the thesis and future directions in the area of EPID *in vivo* dosimetry.

Chapter 2

Background

In this chapter, the production of radiotherapeutic photons is discussed as well as the coordinate systems used in radiotherapy (Section 2.1). The dosimetric response of electronic portal imaging devices (EPIDs) is presented with reference to precision, accuracy, dose range dependence, and dose-rate dependence (Section 2.2). Elements of conventional dose calculation algorithms are discussed (Section 2.3), and summaries of approaches to *in vivo* IMRT and VMAT portal image-based dosimetry are outlined (Section 2.4).

2.1 Physics of radiation therapy

2.1.1 Production of high energy photons

Medical linear accelerators are used to generate megavoltage (MV) energy photon or electron beams in external beam radiotherapy [25]. The description presented below is specific to radiotherapeutic MV photon production.

As shown in Figure 2.1, electrons are first injected in to the linear accelerator system by an electron gun via thermionic emission. The electrons are accelerated across an initial kilovoltage (kV) potential difference. The electrons enter the accelerating waveguide, either a standing or travelling waveguide, located in the linear accelerator gantry. In the waveguide, microwave radiation is used to accelerate electrons to MeV kinetic energies. The microwave radiation is produced by a radio frequency (RF) source (e.g. a klystron), which uses as its input high voltage pulses from a pulse modulator unit.

The narrow beam of monoenergetic MeV electrons that exits the waveguide is steered downwards by a bending magnet (a 270° achromatic bending magnet is shown in Figure 2.1), which directs the electrons down through the treatment head. The electrons strike a high atomic number (tungsten) X-ray target. The result of electrons striking the target is that a wide, continuous spectrum of photons is generated predominantly via bremsstrahlung. Bremsstrahlung occurs when an electron is deflected or scattered by another charged particle (e.g. a nucleus); the acceleration that the electron undergoes during scattering causes the release of a photon in the X-ray range of the electromagnetic spectrum.

The photon intensity distribution resulting from bremsstrahlung events, which are largely forward directed, is then attenuated in a radially-dependent manner by a flattening filter in order to achieve a uniform ("flat") photon beam.

The beam-shaping devices inside the head of a modern linear accelerator include primary and secondary collimators for coarse collimation, and a tertiary multi-leaf collimator (MLC) for fine collimation. The primary collimators are fixed and function as the beam aperture. The secondary collimators are composed of the rectangular $X-$ and $Y-$jaws and are able to rotate about the beam central axis. The $X-$ and $Y-$jaws define the rectangular field size at isocenter. The MLC is used as a final collimator to shape photon beams in order to conform to particular asymmetric shapes or to dynamically modulate the intensity of the radiation beam.

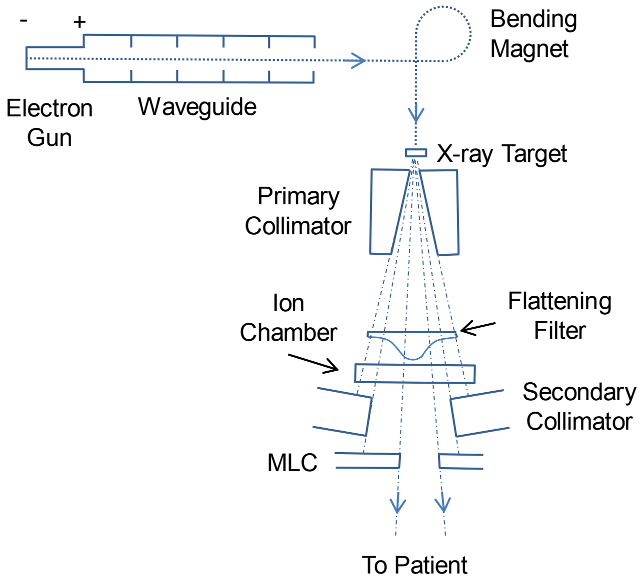

Figure 2.1: Cross-section of linear accelerator head, showing components in the beam direction (top to bottom). The distance from the target to the MLC is approximately 50 cm. The figure is otherwise not to scale.

2.1.2 Treatment unit coordinate system

The International Electrotechnical Commission (IEC) fixed coordinate system is the standard linear accelerator coordinate system that is used in radiation oncology. The IEC fixed coordinate system allows patients to be set up or moved around on the treatment bed in an unambiguous manner. It further provides a common reference system between patient positioning in diagnostic scanning (e.g. CT) and treatment delivery. In Figure 2.2 the orientation of the IEC fixed coordinate system and the EPID coordinate systems are shown with respect to the treatment unit.

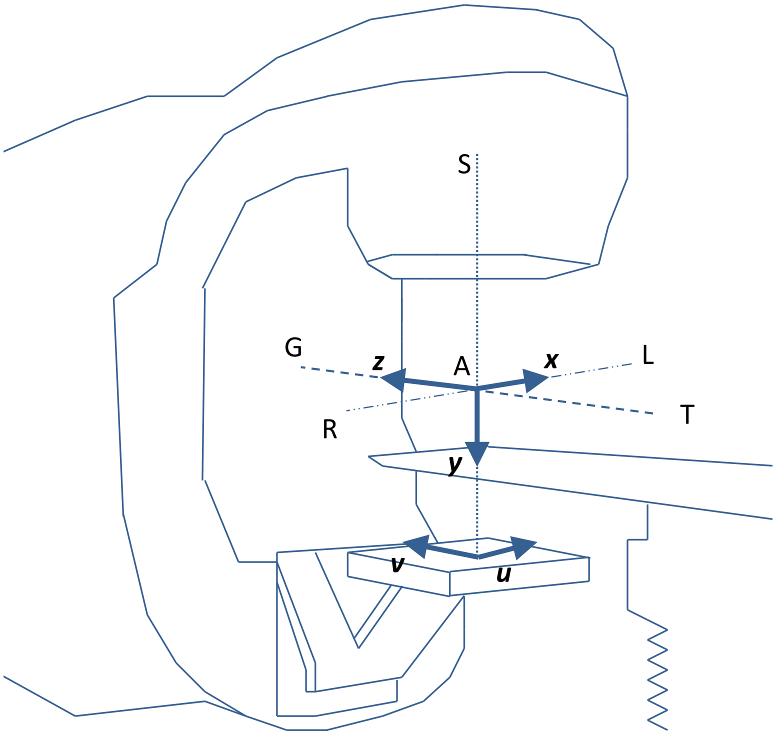

Figure 2.2: Schematic of clinical linear accelerator geometry showing the patient coordinate system (axes x, y, and z) and coordinate system of EPID (axes u and v). The beam central axis is shown by the vertical dotted line S-A, which is also the source-to-axis distance (SAD). The axis of gantry rotation is shown by the dashed line G-T, representing the "gun" and "target" directions respectively.

The IEC fixed coordinate system is intimately related to patient orientation. In Table 2.1, the relationship between the axes and patient orientation is shown. In Table 2.2, the relationship between the three orthogonal patient imaging planes and corresponding IEC fixed coordinate system planes is shown.

Table 2.1: Patient orientation in relation to the IEC fixed coordinate system for a patient positioned head-first with respect to the linac gantry in the supine position.

Patient Orientation	Axis	Patient Orientation	Axis
Left (of patient)	$+x$	Right (of patient)	$-x$
Posterior	$+y$	Anterior	$-y$
Superior	$+z$	Inferior	$-z$

Table 2.2: Principle orthogonal imaging planes in relation to the IEC fixed coordinate system for a patient positioned head-first with respect to the linac gantry in the supine position.

Imaging Plane	IEC Fixed Coordinate System Plane
Axial	xy-plane
Coronal	xz-plane
Sagital	yz-plane

The orientation of the IEC fixed coordinate system is set with respect to the isocenter (the point 'A' in the Figure 2.2). The EPID coordinate system is fixed with respect to the plane defined by the EPID detector surface. As the linear accelerator gantry and EPID rotate about the isocenter, the EPID $v-$axis is parallel to the IEC $z-$axis; however, the u-axis is only parallel to the IEC $x-$axis at gantry angle zero.

For the purpose of this thesis, the EPID coordinate system is chosen have the axis labels u and v in order to avoid ambiguity with the patient coordinate system. An (x, y, z) coordinate labelling is often used for the EPID position, where x and y have been replaced with u and v respectively, while z is vertical distance from isocenter that is related to the source-to-detector distance (SDD) notation that is used in this thesis.

2.1.3 Dosimetry

A fixed coordinate system is essential for the patient to be set up correctly and unambiguously on the day of treatment. Before a patient may be treated with radiation therapy, the absorbed dose due to the linear accelerator radiation must also be correct. The absorbed dose output is measured on a daily, weekly, monthly, and annual basis using accurate standards. The linear accelerator output is examined for deviations from the calibration dose of 1 cGy per monitor unit (MU) to a depth of $d_m = 1.5$ cm in water at 100 cm SAD (for a 10×10 cm^2 field size). The monitor unit is a measure of linear accelerator output, measured by the ion chambers in the linear accelerator head shown in Figure 2.1.

To measure the absorbed dose, a wide variety of dosimeters may be employed. Ionization chambers (ion chambers), silicon diodes, radiochromic film, thermoluminescent detectors (TLD), metal-oxide-semiconductor field-effect transistor (MOSFET) detectors, and EPIDs are all used for dose measurements. Each type of dosimeter generally has a preferred use. For example, ion chambers are calibrated against standards to monitor the linear accelerator output whereas film might be used to measure absorbed dose across a plane in IMRT pre-treatment verification. In this study, only ion chambers and EPIDs are investigated; an ion chamber was used to provide an absolute dose calibration for the EPID.

A properly calibrated ion chamber is the "gold standard" in MV photon dosimetry. The ion chamber used in this study was a compact, thimble ion chamber; the details of the model are provided in Chapter 3. The chamber has an electrode (made from an air-equivalent plastic) surrounded by a very small (0.13 cc) active volume. The electrode is held at a constant positive voltage relative to the chamber wall. High energy photons interact with the air within the chamber cavity, causing electrons to be liberated. These electrons are drawn towards the electrode which collects the electrons. The charge collected is proportional to absorbed dose. The constant of proportionality can be determined by a calibration measurement where the charge liberated due to a known dose is recorded and used to calculate a dose-per-unit charge ratio.

The second dosimeter discussed in this study is the EPID. This device is discussed in detail in Section 2.2 below.

2.2 Electronic portal imaging devices

In radiotherapy departments where EPIDs are used routinely, EPIDs are primarily used to acquire images in order to verify patient setup ahead of treatment [26]. Over the past twenty five years, EPID technology has evolved greatly and surpassed film as the portal imaging standard.

Portal images formed with MV photon beams typically suffer from poor contrast [26]. At MV energies, Compton scattering is the dominant photon interaction in lower atomic number materials (tissue-like materials). The Compton mass attenuation coefficient varies approximately as the electron density, which means that good contrast is only obtained if the beam passes through large amounts of high or low electron density material (e.g. bone and air respectively). Any limitations of contrast in portal imaging, however, are not important in the context of EPID dosimetry.

2.2.1 Detectors

EPID technology has changed significantly over the past two decades. The early 1990s saw the development of matrix ion chambers, which were direct radiation detectors. The next step was the introduction of indirect detectors, starting with camera-based detectors which converted high-energy photons in to visible light for detection. Solid state detectors, another form of indirect detector, are now are the portal imaging standard. The three classes of EPIDs are discussed briefly in this section.

Matrix ion chambers

Matrix ion chambers were among the first simple electronic detectors developed for portal imaging [27]. These devices consist of a matrix of electrodes immersed in 2,2,4-trimethylpentane, an ionization medium. The charge collected by each electrode following exposure to the photon beam is mapped to a greyscale value, providing electronic images of exit radiation beams. In addition to suffering from poor spatial resolution, these devices require a high exposure to generate an acceptable image (an order of magnitude higher than modern EPIDs) [26, 28].

Camera-based detectors

Camera-based detectors offer the advantage of real-time, continuous imaging during radiation therapy [29]. Exit radiation beams are received by a metal plate and phosphor combination. Electrons released in the metal plate cause the adjacent phosphor to emit photons in the visible range of the electromagnetic spectrum. The light emitted is reflected by a mirror oriented at 45° into a lens perpendicular to the beam direction, and the signal is recorded by a camera attached to the lens or displayed by the imaging unit.

Solid-state detectors

Solid state detectors [30] have nearly completely replaced matrix ion chambers and camera-based detectors in modern radiotherapy. The short exposures (on the order of 1 MU) required to generate high quality images, high spatial resolution, and online integration with linear accelerator systems have made these devices the portal imaging standard.

Solid state detectors are located beneath a copper plate and phosphor layer (e.g. Gd_2O_2S:Tb). The solid state detectors are typically composed of hydrogenated amorphous silicon (a-Si) photodiodes and thin-film transistors. The a-Si photodiodes are made of two adjacent layers of $n-$ and $p-$ doped silicon under reverse bias voltage.

High energy photons that interact with the copper plate release lower-energy recoil electrons. These electrons interact with the phosphor and cause it to exhibit phosphorescence, the release of visible light. The a-Si flat panel light detector measures the amount of light incident on the detector. When the visible light interacts with the silicon layer, an electron-hole pair is created. The electrons generated in the electron-hole pair creation are drawn to the cathode, generating a current. This current is integrated and the charge is recorded. The charge generated during this process is collected, stored, and transferred to the display where the image is formed based on the charge at each detector element (pixel).

2.2.2 Design and materials

The device used in this study is the Varian aS1000 EPID (Varian Medical Systems, Palo Alto CA). The design of the aS1000 EPID is similar to its predecessor, the Varian aS500, and follows the same basic construction. Its composition is as follows [31]. The components are listed in the direction of the beam:

- 1.6 mm of epoxy cover plate
- 9 mm of circuitry and Rohacell (a low density foam)
- 1 mm copper plating
- 0.4 mm Gd_2O_2S:Tb (gadolinium oxysulphide doped with terbium) phosphor
- a-Si flat panel light detector (photodiodes and thin-film transistors)
- Glass panel, rear detector housing, and cables

In Figure 2.3, a graphical representation of the EPID construction in the direction of the radiation beam is shown (beam enters at top of figure and exits at bottom of figure).

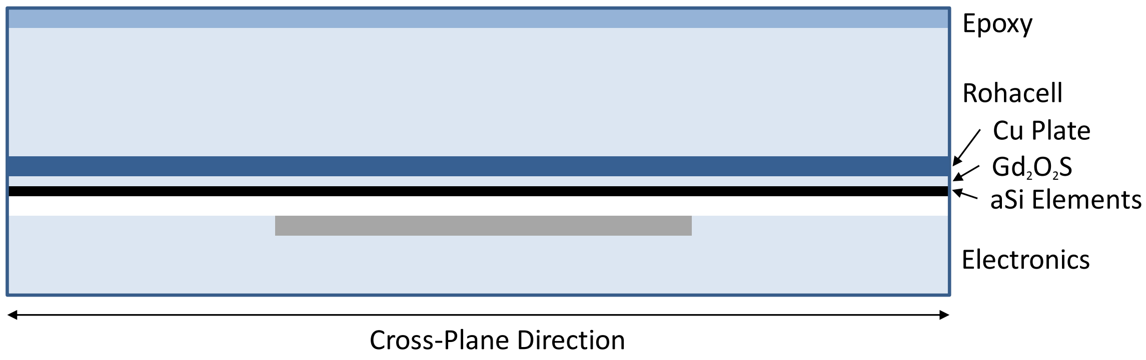

Figure 2.3: Cross section of the Varian aS1000 portal imager showing the components listed in the text. Figure not to scale.

The aS1000 EPID is attached to the linear accelerator by the Varian Exact arm (E-arm). The E-arm controls the position of the EPID and ensures that the centre pixel region of the EPID is consistently aligned with the beam central axis. The E-arm allows for the portal imager to have a set-up reproducibility of less than 2 mm in each of three orthogonal axes (as specified by the manufacturer) [32]. Studies have measured the EPID sag due to gravity as the gantry rotates [33]. The EPID sag of the aS1000 portal imager on an E-arm was variable from institution to institution. The EPID displacement due to sag as the gantry rotated had a range of [-0.6, 2.0] mm in the cross-plane direction and a range of [0.0, 0.9] mm in the in-plane direction [33].

The E-arm construction and layout has the consequence of introducing a spatially variable radiation backscatter effect that is not evident on other EPIDs. While this effect is negligible when MV imaging used for positional purposes, it can be profound for EPID dosimetry [34]. A schematic of the aS1000 with E-arm components is shown in Figure 2.4. The difference in backscatter material beneath the detector on the target half (negative EPID v-axis) and the gun half (positive EPID v-axis) causes the detector elements on the target half record a higher signal.

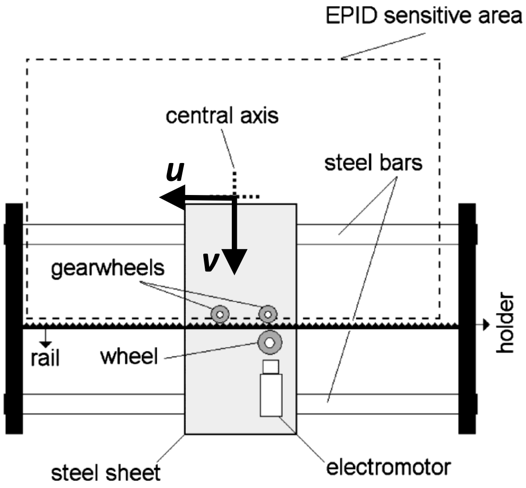

Figure 2.4: Schematic of the Varian aS1000 and E-arm components as viewed from beneath the EPID. Reprinted from Rowshanfarzad [35], with permission of the AAPM. Figure not to scale. The axes u and v are as described in Figure 2.2.

2.2.3 Dosimetric characteristics

The Varian X-ray Imaging (XI) system is the node within the TrueBeam (v1.6, Varian Medical Systems, Palo Alto, CA) linear accelerator system that processes MV image data [36]. The XI node links the MV acquisition system, which is composed of the image detection unit and digitizer unit, with the treatment unit's database.

The XI system is able to acquire single "radshot" setup images, continuous (cine) images, and dosimetry (or "integrated") images. Integrated images are acquired in what is termed unsynchronized mode. In this mode, the image readout is not synchronized with beam pulses; the image is acquired until beam off so that the system registers the complete beam signal.

Following the beam on signal, the image detection unit acquires image frames at a frequency of approximately 10 frames per second. Each frame is transferred to the digitizer unit, where it is converted from an analogue signal to a digital signal. The XI node receives the frame, and performs offset and gain corrections for each frame. The acquisition, digitization, and correction process continues until the beam is turned off. The frames are summed in order to create a final image in integrated mode. The XI node transfers the image to the treatment unit's database where it can be viewed or analyzed.

The signal of the final portal image is appealing for dosimetry purposes. The integrated image describes the intensity variation of the photon beam within a plane. The absolute magnitude of each integrated pixel value is reproducible (the same fluence produces a reproducible signal) and the integrated pixel value proportional to absorbed dose when appropriately corrected. It is for these two reasons that portal images can be used as dosimeters [12]. However, like any dosimeter, the EPID ought to be evaluated on the basis of its merits to understand its usefulness and its shortcomings. Attix outlines the essential characteristics by which a dosimeter can be evaluated [37]. The precision and accuracy, dose range, and dose rate range are important factors when detailing the dosimetric capability of electronic portal imaging devices.

Precision and accuracy

The reproducibility of measurements under fixed reference conditions is important for assessing any dosimeter; this quality is generally referred to as the precision of a device. It has been reported that readings made with the aS500 EPID are precise to within 2% over the course of four months [38]. Measurements of the integrated signal per monitor unit on an aS1000 EPID were tracked over the course of the clinical study performed in this thesis. These measurements are shown in Figure 2.5(a) and they demonstrate that from October 2012 to March 2013, the integrated EPID signal was stable to within 1% of the baseline signal.

The accuracy of EPIDs with respect to gold-standard dosimeters (e.g. ion chambers) is strongly dependent upon the EPID calibration conditions. Even with a rudimentary calibration procedure, the relative EPID derived doses can be accurate to within 3% for open and wedged fields and accurate to within 5% for IMRT fields when no material is in the path of the beam [12]. This baseline accuracy can be significantly improved with the inclusion of empirical correction factors.

Dose range

Varian product literature describes the dose range of the aS1000 portal imager; a minimum exposure of 1 MU is required to generate an image and the maximum image exposure is 999 MU in clinical mode (a software limit) [32].

Ideally, a dosimeter's response should be linear with respect to dose [37]. A linear dose response facilitates calibration, requiring simply one reference measurement if the dosimeter is appropriately zeroed. (Note that this is just an ideal quality; ra-

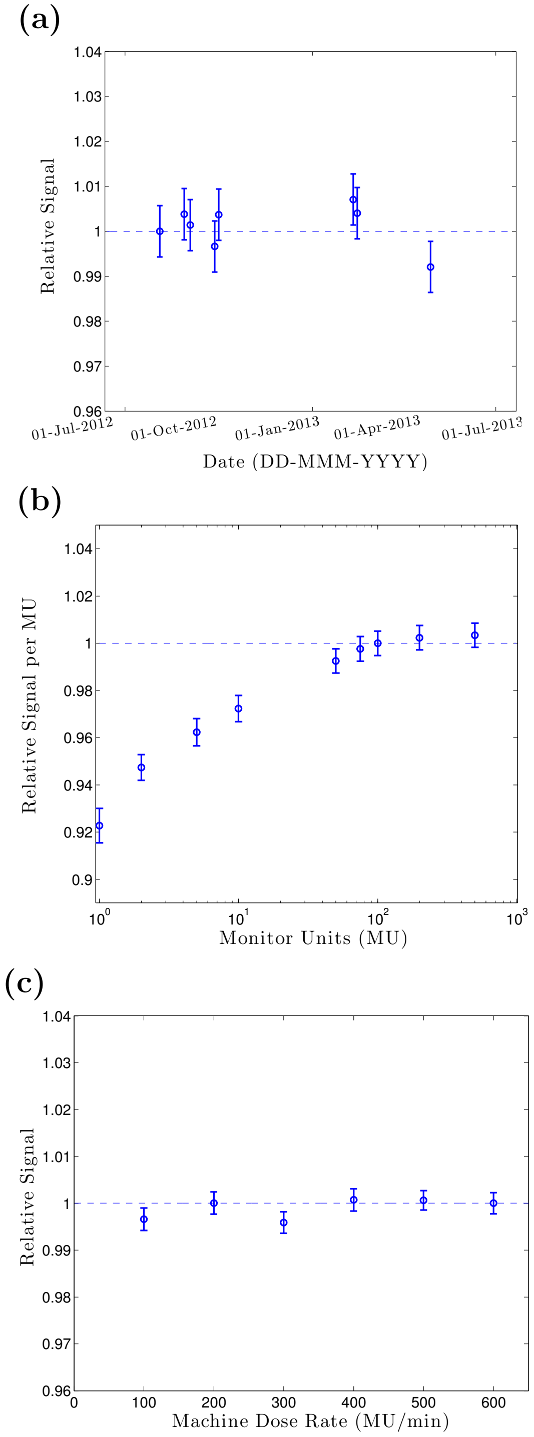

Figure 2.5: Relative signal of the EPID as measured inside ROI along the central axis as a function of: **(a)** Gregorian date, normalized to signal of 01-Oct-2012, in order to quantify EPID precision, **(b)** monitor units, normalized to signal at 100 MU, in order to quantify EPID linearity, **(c)** nominal machine dose rate, normalized to signal at 600 MU/min, in order to quantify EPID dose-rate dependence.

diochromic film, for example, is an excellent dosimeter but involves a more complex calibration as the dose response is non-linear.)

The portal image signal as a function of dose (represented by monitor units) has been documented, and the linearity of the EPID has been well established for acquisitions with a high number of monitor units (MU) [12]. In Figure 2.5(b), the portal image signal per MU is shown as a function of the nominal monitor units. For acquisitions with a low number of monitor units (less than 10 MU), up to 8% of the integrated signal is "lost" compared to irradiations with a higher number of MU.

McDermott et al. [39] analyzed the above "ghosting" effect which is evident in amorphous silicon EPIDs. The ghosting effect (which includes the combined effects of both image lag and gain ghosting) arises as a result of the nature of the aSi devices. When charge is liberated in the silicon layer, it can be collected in unfilled "traps." At shorter exposures (less than 25 MU), this effect is particularly evident since more charge is trapped relative to the charge that is generated; however, for longer exposures (more than 25 MU), the traps become saturated and an equilibrium is established.

For acquisitions of greater than 50 MU, the portal image signals per MU agree to within 1%. This agreement is important for the implementation of EPID dosimetry clinically since more than 50 MU are used to treat the vast majority of IMRT fields.

Dose rate range

An ideal dosimeter should measure a dose that is independent of the rate at which that dose was accumulated. The manufacturer-specified supported dose rate for the aS1000 ranges from 50 MU/min to 600 MU/min [32]. The relative portal image signal for a fixed number of MU (50 MU) was observed to be constant to within 0.5% over this dose range as shown in Figure 2.5(c). The signals were normalized to a dose rate of 600 MU/min since this was the dose rate at which dose calibration images were acquired; this is also the dose rate that is employed for clinical IMRT treatments at the BCCA-VIC on Varian TrueBeam units.

2.3 Radiation modelling

2.3.1 Treatment planning systems

Various strategies have been devised to simulate the complex interactions of ionizing radiation with matter. The pencil-beam convolution algorithm (PBC), superposition/convolution methods (SC), and Monte Carlo simulation (MC) are three examples of model-based dose calculation systems that are used in modern radiation therapy. Only the pencil-beam convolution and the anisotropic analytical algorithm are presented in this section as Monte Carlo calculations were not used in this study. Monte Carlo calculations can be considered a separate class of dose calculation system as they simulate fundamental particle interactions explicitly unlike the previous two, model based, systems.

Pencil-beam convolution

Pencil-beam convolution algorithms, described by Ahnesjö et al. [40], were devised as an alternative to conventional correction-based algorithms. The pencil-beam convolution algorithm models a radiation beam as being composed of a set of infinitesimally small beams (so-called "pencil beams"). Each pencil beam is convolved with a kernel that simulates scattering radiation at a depth z in the patient. The total dose is therefore the sum of the dose contributed by each pencil beam.

A representative pencil-beam convolution method for dose calculation in a homogeneous water phantom, $D(x, y, z)$, presented by Storchi et al. [41], can be written as:

$$D(x,y,z) = \frac{(f+z_{ref})^2}{(f+z)^2} \int_{-\infty}^{+\infty} \int_{-\infty}^{+\infty} F(x',\ y')\ P_{int}(x',y',z)\ K(x-x',\ y-y',\ z)\ \mathrm{d}x'\mathrm{d}y' \tag{2.1}$$

where f is the source-to-surface distance, z_{ref} is the calculation reference depth, z is the calculation depth, $F(x, y)$ is the field intensity function, $P_{int}(x, y, z)$ is an intensity profile, and $K(x, y, z)$ is a rotationally symmetric kernel that incorporates the scatter and attenuation of a pencil beam in water. Note that (x, y, z) is a beam-oriented orthogonal coordinate system (with z is in the direction of the beam), not the IEC fixed patient coordinate system.

In the first step of the PBC, the field intensity function at a plane is multiplied by the intensity profile, which describes the off-axis variation of the beam. The resulting quantity is known as the modified fluence. The modified fluence is convolved with a depth-dependent dose deposition kernel to calculate the absorbed dose.

PBC algorithms suffer from inaccuracies at field edges, at interfaces of two media (e.g. bone and tissue interfaces), and in high dose gradients. While the PBC algorithm has been gradually supplanted clinically by SC algorithms, is important for understanding the basis of many EPID dose verification models.

The PBC is important in the context of EPID dosimetry as a dosimetry portal image contains a measure of the field intensity function, $F(x, y)$, once attenuation and scatter due to the patient in the beam have been removed. From the recovered field intensity function, it is possible to use a PBC model to calculate the dose at a plane in the patient. This is accomplished by convolving the measure of $F(x, y)$ with a scattering kernel ($K(x, y)$). As with the PBC algorithm, a spatially invariant kernel is used; therefore, convolution can be performed quickly using the Fourier transform (FT) operation.

Superpositon/Convolution

Today, superposition/convolution techniques are the standard in radiation therapy treatment planning. The treatment planning system Eclipse (v10.0, Varian Medical Systems, Palo Alto CA) incorporates one such implementation, the Anisotropic Analytical Algorithm (AAA), into photon dose calculations. AAA represents an improvement over conventional PBC algorithms for radiation therapy dose calculations [42]. It is generally considered to be accurate to within 1%-2% in homogeneous media (e.g. water) and within 2.5% in the presence of common, smaller inhomogeneities [42–44].

As with the PBC model, in AAA the photon beam is divided into a subset of smaller beams, known as "beamlets". An energy deposition density function is used to characterize attenuation of each beamlet through the medium, which scales the calculation depth in water-equivalent terms. Photon scatter is calculated by the multiplication of the energy deposition density function with a scatter kernel that is generated based on material data along the path of the beamlet. The lateral distances of the kernel are scaled according to the water-equivalent lengths of neighbouring voxels; this lateral scaling accounts for differential scattering characteristics of heterogeneous media. In addition to the contribution of photon scatter, additional considerations are made in the AAA to account for the dose due to extra-focal photons and for contaminant electrons in the calculation of the absorbed dose.

The total volume dose is calculated by summing the contribution of each beamlet; this is the "superposition" aspect of this model.

2.3.2 Comparing dose distributions

In order to quantify the accuracy of a dose distribution, robust tools must be available to evaluate a calculated or measured dose distribution against another in multiple dimensions. This might include, for example, comparing a dose distribution measured using radiochromic film against a dose plane from the treatment planning system (TPS). Several strategies have been formulated for the quantitative evaluation of radiation dose distributions. The most widely used comparison in medical physics is the γ-index evaluation, first proposed by Low et al. [45]. The γ-index evaluation incorporates two acceptance criteria when comparing dose distributions: a distance-to-agreement parameter (Δd_{DTA}) and a dose difference parameter (ΔD_{DD}). The DTA and DD parameters represent the maximum distance at which two points can be judged to agree and the maximum acceptable dose difference respectively.

To understand the γ-evaluation, first consider a single voxel of interest in a volume at $\vec{r}_a$. For two dose distributions, D_a and D_b, that are calculated for a given volume, the Γ matrix specific to the point of interest $\vec{r}_a$ is calculated according to:

$$\Gamma(\vec{r}_a, \vec{r}_b) = \sqrt{\frac{|\vec{r}_a - \vec{r}_b|^2}{\Delta d^2_{DTA}} + \frac{|D_a(\vec{r}_a) - D_b(\vec{r}_b)|^2}{\Delta D^2_{DD}}} \tag{2.2}$$

where $|\vec{r}_a - \vec{r}_b|$ is the matrix that describes the distance from the point of interest $\vec{r}_a$ to a generic voxel $\vec{r}_b$, and $|D_a(\vec{r}_a) - D_b(\vec{r}_b)|$ is the matrix that describes the dose difference between distributions D_a and D_b. For ease of computation, the Γ value is typically only computed within a predefined neighbourhood of the point of interest.

The γ-index that is assigned to the point $\vec{r}_a$ is given by the value that minimizes the Γ-matrix:

$$\gamma(\vec{r}_a) = \min\{\Gamma(\vec{r}_a, \vec{r}_b), \forall\ \vec{r}_b\} \tag{2.3}$$

This calculation is repeated for all points within a plane or volume, depending on which is of interest. A γ-value at a pixel is considered to have "passed" - or satisfied the combined distance-to-agreement and dose difference criteria - if $\gamma < 1.0$.

All $\gamma-$evaluations performed in this study were carried out with $\Delta d_{DTA} = 3$ mm and $\Delta D_{DD} = 3\%$ of the global dose maximum. The $\gamma-$evaluation was only performed on those pixels with greater than 10% of the maximum dose in the plane (the "threshold" value). A recent survey showed that the 3%/3mm criteria is the most popular $\gamma-$evaluation criteria used clinically for IMRT QA, while the threshold value varies significantly [46].

The $\gamma-$evaluation technique can break down in the presence of large amounts of noise in either a reference of evaluated dose distribution [47] and analysis results vary significantly based on the detector sampling (number of detector elements per unit area or volume) [48].

Other comparison techniques include the χ-evaluation, presented by Bakai et al. [49]. The χ-evaluation follows from the γ-evaluation, however, it is calculated using a gradient-dependent function rather than a search method like the γ-evaluation. This evaluation is used at the BCCA-VIC for pre-treatment EPID dosimetry; however, the γ-evaluation has been used in this study to facilitate comparisons with other studies.

2.4 Recent advances in EPID dosimetry

The feasibility of EPID dosimetry has been studied since the first ion chambers matrix EPID was developed. However, with the advancement of the technology behind these devices - in particular the ability of aSi EPIDs to rapidly provide high resolution, complete digital images - interest in EPID dosimetry has soared [13]. Several of the more fundamental and more recent transit EPID dosimetry studies that pertain to this thesis are described in this section. The review of van Elmpt et al. provides a comprehensive review on the literature of EPID dosimetry as of 2008 [13].

2.4.1 IMRT transit verification

Transit verification of IMRT treatments can be performed using two closely related methods: (1) Either the dose at the level of the portal imager can be measured and compared to a predicted value (the "portal dose image" verification method), or (2) the EPID signal can be back-projected through a model of the patient in order to estimate the patient dose ("*in vivo*" verification).

In the first class of EPID dosimetry, Berry et al. [50] extended the portal dose image (PDI) prediction technique of van Esch et al. [51] in order to predict the dose at the level of the portal imager following transmission of the beam through the patient. The study of Berry et al. [50] examined the prediction algorithm for a range of fields and phantom geometries and it was shown to be highly accurate. However, a limitation of portal dose prediction and verification techniques is that it is not immediately evident how a difference in portal dose can be translated to a difference in patient dose.

The second class of IMRT transit dosimetry (*in vivo* verification) uses a measure of the portal image signal to back-project the radiation field through a model of the patient in order to estimate the dose to the patient during treatment—a quantity that is much more clinically intuitive. IMRT *in vivo* dosimetry has been developed extensively at the Netherlands Cancer Institute Antoni van Leeuwenhoek Hospital

(NKI-AVL) [23, 26, 52–55]. At the NKI-AVL, *in vivo* EPID dosimetry has been refined and modified extensively over the past decade, and has been incorporated into an institutional clinical routine. Two- or three-dimensional verification is performed using either a measured or calculated patient transmission factor, and the back-projected dose is compared to the planned distribution using a γ-evaluation.

This thesis seeks to develop and validate a portal imager-based patient dosimetry system based on the model that has been laid out by the NKI-AVL.

2.4.2 VMAT transit verification

Volumetric modulated arc therapy (VMAT) began to gain widespread clinical use following a proof-of-principle of intensity modulated arc therapy by Otto in 2008 [5]. The review of van Elmpt et al. [13] included information on 3DCRT and IMRT, but was not recent enough to include a description of EPID dosimetry strategies employed in VMAT *in vivo* treatment verification.

Slorasek et al. [56] have used single integrated portal images to calculate the *in vivo* dose to isocenter for VMAT treatments. In their solution, the plan was first delivered to a phantom and a reference phantom dose measurement was made using an ion chamber prior to acquiring the portal image. The portal image signal at a region of interest along the central axis of the EPID following transmission through the patient and the phantom dose measurement were used to estimate an *in vivo* isocenter dose.

The ideal portal image acquisition mode for VMAT treatment is dosimetric cine mode, which provides angularly resolved images at pre-defined intervals. This imaging mode was first validated for dynamic arc IMRT dosimetry by McCurdy and Greer [57]. Cine imaging has been used to calculate the *in vivo* isocenter dose by relating the signal along the central axis of each image to isocenter in the patient in dynamic arc radiaton therapy [58, 59]. Mans et al. [24] have used cine images to calculate a complete three-dimensional patient dose following VMAT treatment based on the angularly resolved information contained in cine portal images.

Cine imaging appears to be the optimal image acquisition mode for EPID VMAT pre-treatment verification and EPID *in vivo* dosimetry as it provides the requisite angular information. However, in the Varian TrueBeam treatment mode dosimetric image acquisition is limited to single integrated portal images over an arc. Cine-images are not acquired with dosimetry characteristics. This limitation forms the basis for the *in vivo* VMAT dosimetry technique that is developed in this thesis.

Chapter 3

Materials and Methods

In this chapter, a method of EPID dosimetric calibration and subsequent back-projection is presented (Sections 3.1 - 3.4). The experiments that provided the parameters for the dose back projection algorithm are discussed. Finally, the adaptation of the IMRT dose back-projection for VMAT treatments is presented in Section 3.5.

A Varian TrueBeam linear accelerator with a 120-leaf Millennium multi-leaf collimator (MLC) was used to deliver 6 MV photons in this study. A Varian aS1000 amorphous-silicon (a-Si) EPID was attached to the linear accelerator and was set to 150 cm source-to-detector distance (SDD) for all irradiations unless otherwise noted. The dosimetry imaging mode was used to acquire a single integrated electronic portal image for each field (IMRT) or for each arc (VMAT). In this imaging mode, each pixel value is displayed as a rescaled 16-bit integer, displayed in Digital Units (DU). A rescale slope value ($m_{rescale}$) was encoded in the portal image header information and was used to relate the scaled pixel value to the true integrated signal, PV (in Calibrated Units, CU). The rescale slope value contains a measure of the number of frames that were recorded and the user-defined calibration factor. For each EPID pixel ij, flood-field (FF_{ij}) and dark-field (DF_{ij}) image corrections were applied automatically to the raw portal image (PV_{ij}^{raw}) by the image acquisition module to give the corrected integrated signal (PV_{ij}) as follows [12]:

$$PV_{ij} = \left[\left(\frac{PV_{ij}^{raw} - DF_{ij}}{FF_{ij} - DF_{ij}} \right) \cdot [FF_{ij} - DF_{ij}]_{mean} \right] \cdot m_{rescale} \tag{3.1}$$

The flood-field image is acquired with a large field and it is used to correct for individual pixel responses. The dark-field image is acquired without radiation and is used to correct for background signals that are recorded in the absence of radiation.

The sensitive area of the aS1000 portal imager measures 40 × 30 cm^2 ($u \times v$) and acquired images have a display resolution of 1024 × 768 pixels. Each pixel therefore has an area of 0.0391 × 0.0391 cm^2. No additional build-up material was placed above the sensitive area of the EPID.

Portal images were analyzed using MATLAB (v7.10.0, Mathworks, Natick, MA) software. For the purpose of this analysis, the portal images were resampled to 512 × 384 pixels to decrease calculation time while still maintaining an image with excellent resolution. The effective pixel area was therefore 0.078 × 0.078 cm^2. Finally, images were padded with the minimum portal image pixel value to create a square image of 768 × 768 pixels. This padding is done in order to facilitate implementation of the Fast Fourier Transform (FFT), to prevent unphysical periodic artifacts, and to improve deconvolution accuracy for very large field sizes (i.e. those fields that extend close to the edge of the image) [23].

An IC-10 ionization chamber (0.13 cc active volume, Wellhöfer Dosimetrie, Germany) was used to calibrate the portal imager for dosimetric use and was the standard against which all portal image doses along the central axis were compared. The treatment planning system (TPS) used in this study was Varian Eclipse. The TPS, which has previously been validated at extended source-to-surface distances [60], was the standard against which all portal image beam profiles were compared.

In each of the following sections of this chapter, (1) an overview of each component of the back-projection algorithm is presented, (2) an outline of the experiments that were performed in order to characterize the component is discussed, and (3) a description of how the component is modelled in the back-projection algorithm is outlined.

In Figure 3.1, the process of converting the portal image to dose at the isocenter plane in the patient is presented. The corresponding section that describes each major step is labelled.

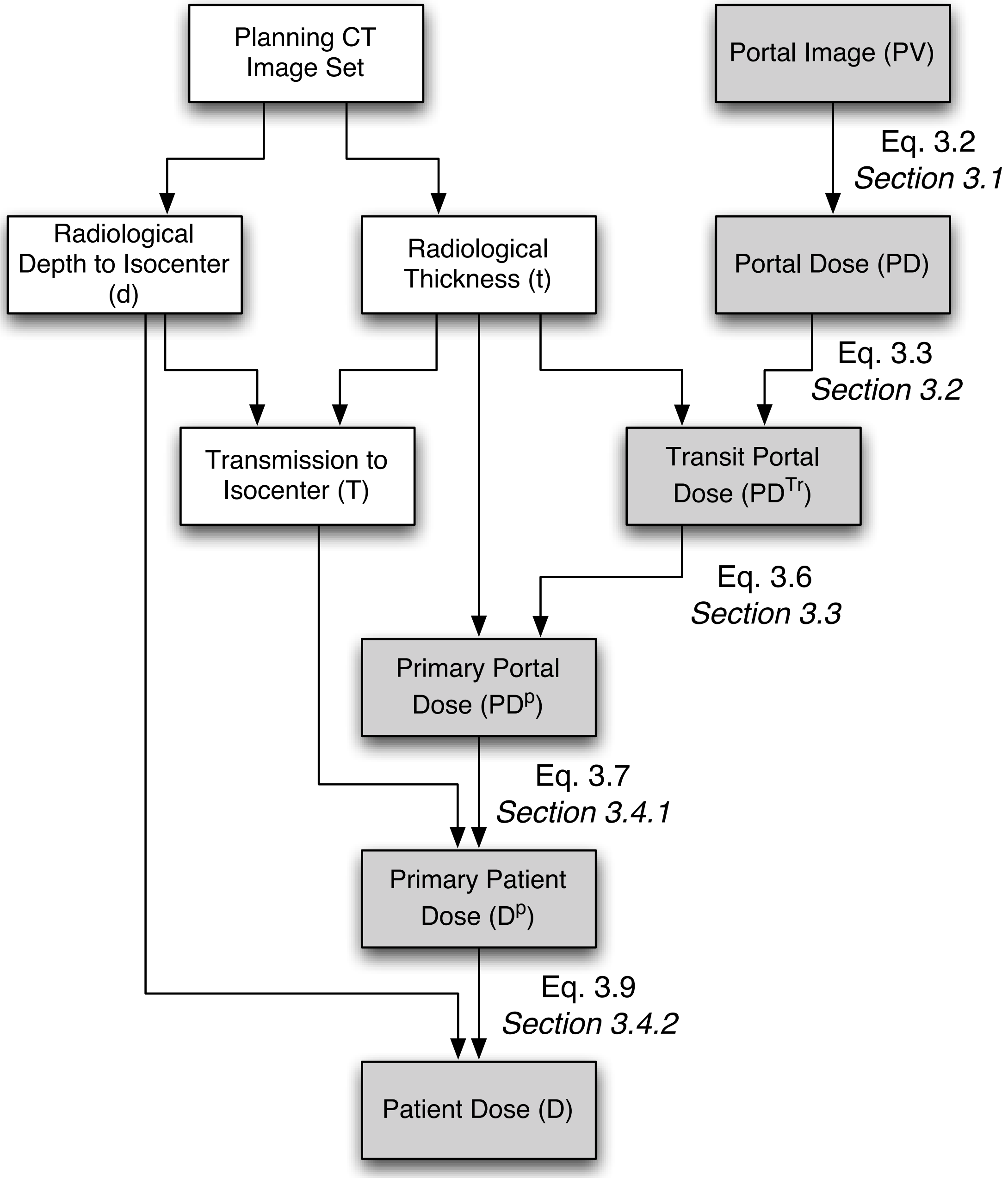

Figure 3.1: Flowchart describing process of patient dose reconstruction from initial portal image and patient planning CT data. The section and equation describing the operations required to progress to the next step are shown.

3.1 EPID dose calibration

3.1.1 Absolute dose calibration

Before an EPID can be used for dosimetric purposes, it must be calibrated in terms of absolute dose. The aS1000 EPID has approximately 0.8 cm of water-equivalent attenuating material above the active detector layer. However, for simplicity and for the purpose of an accurate dose calibration, it is acceptable to model the detector elements as if they were at a water-equivalent depth of $d_m = 1.5$ cm [61]. Since beam cross-sectional profiles are similar at $d = 0.8$ cm and $d = 1.5$ cm, and the calibration dose must ultimately be referenced to d_m, this is a valid procedure.

To determine a reference signal-to-dose calibration, the EPID was irradiated with a 10 × 10 cm^2 field that would deliver a dose of 100 cGy at a point along the central axis of the beam at a depth $d_m = 1.5$ cm in water at SDD = 150 cm. The mean value of the integrated portal image signal, measured in Calibrated Units (CU), of a region of interest (ROI) measuring 5 × 5 pixels (3.9 × 3.9 mm^2) along the central axis was recorded. This reading was then related to the dose along the central axis at $d_m = 1.5$ cm to calculate the absolute dose calibration factor,

$$g = \frac{\text{Calibration Dose (cGy)}}{\text{ROI Signal (CU)}},$$

which was the dose per pixel value calibration according to which all pixels across the area of the imager were scaled.

3.1.2 Lateral scatter and optical glare

The design of an amorphous silicon EPID causes blurring of the incident fluence and a field-size dose dependence that differs from that ideally measured by water. The blurring is caused by photon scattering in the high atomic number materials of the EPID and the isotropic emission of optical photons by the phosphor [62]. Radiation that is scattered within the EPID does not behave in a water-equivalent fashion as the device is constructed with high atomic number elements in order to increase the signal-to-noise ratio. Furthermore, large field sizes contain a proportionally higher fraction of low energy photons which the EPID responds disproportionately to [23, 63].

To characterize the EPID field-size dependence, square fields - ranging from 4 × 4 cm^2 to 18 × 18 cm^2 - were delivered to the EPID with no additional material in the path of the beam. Larger field sizes were not considered since at a SDD of 150 cm or greater these fields extend beyond the sensitive area of the EPID. The mean value of the portal image signal within a region of interest measuring 5 × 5 pixels (3.9 × 3.9 mm^2) along the central axis was recorded for each field. The corresponding dose measured in a water phantom at $d_m = 1.5$ cm at the same source-to-detector distance (SDD) was recorded for each field size.

A deconvolution was performed to correct for the difference in lateral scatter and remove the optical glare in order to obtain an equivalent dose to water at the level of the portal imager. An empirical EPID lateral scatter and glare kernel (${K_{ij}}^{we}$) was developed such that when the kernel was deconvolved from portal images, the resulting dose distributions matched those that would be measured in a water phantom.

The kernel that was chosen had a similar dependence to that used by Wendling et al. [52], which was of the form $\exp(r)/r^2$:

$${K_{ij}}^{we}(r_{ij}) = \begin{cases} A_1 \cdot \exp(-\alpha\ r_{ij})/r_{ij} & \text{if } r_{ij} > 0 \\ A_2 & \text{if } r_{ij} = 0 \end{cases}$$

In this kernel, r_{ij} is the radial distance in centimeters from the centre of the portal image. A_1, A_2, and α are the optimized kernel parameters, chosen such that the squared difference between TPS and EPID signals was minimized over the field size range investigated. Deconvolved portal image doses were validated against TPS dose calculations for agreement along the central axis and in the penumbra region over a range of field sizes from 4 × 4 cm^2 to 18 × 18 cm^2.

The deconvolution calculation was implemented using a Wiener deconvolution filter to reduce noise amplification in the final image. The measured portal image signal, $s(x, y)$, can be modelled in the spatial domain as the convolution ($\otimes$) of the scattering function, $k(x, y)$, and a signal that would be measured in water ("water-equivalent signal"), $w(x, y)$, plus a general noise component, $n(x, y)$:

$$s(x, y) = w(x, y) \otimes k(x, y) + n(x, y).$$

By the Convolution theorem, the Fourier transform (FT) of the measured signal, $S(f, g)$ (capital letters denote Fourier-transformed functions), is given as the product of the FTs of $w(x, y)$ and $k(x, y)$ plus the FT of $n(x, y)$.

$$S(f, g) = W(f, g) \cdot K(f, g) + N(f, g).$$

The Wiener deconvolution is defined as follows [64], in order to calculate the FT of the water-equivalent signal:

$$W(f,g) = \frac{S(f,g)}{K(f,g)} \cdot \Phi(f,g),$$

where $\Phi(f,g)$ is the optimal filter defined as:

$$\Phi(f,g) = \frac{|S(f,g)|^2}{|S(f,g)|^2 + |N(f,g)|^2}.$$

A water-equivalent signal is then recovered by taking the inverse FT of $W(f,g)$. The deconvolution was performed using the Fast Fourier Transform (FFT) and Inverse Fast Fourier Transform (IFFT) commands in MATLAB.

3.1.3 Additional dosimetric corrections

An empirical correction (U_{ij}), linear in radial distance from the centre of the portal imager, was applied to the portal image in order to reintroduce the off-axis fluence behaviour of the radiation beam that is removed during the flood-field correction. The correction factor was as follows,

$$U_{ij} = u_1 r_{ij} + u_0,$$

where u_1 and u_0 are the slope and $y-$intercept respectively of the off-axis term.

A second empirical correction, developed by Berry et al. [34], was applied to the portal image to account for radiation backscattered from the imager support arm (E-arm). The correction is a field-size dependent factor that was quantified as a function of the $Y1$ jaw size for open, square fields. A modification to this correction for the purpose of this study, where the collimator angle is not necessarily zero, was made: the $Y1$ jaw size was replaced with the equivalent length of the radiation field in the inferior $(-u)$ direction, known as Y_{eq}.

The backscatter correction factor (P_{ij}) was defined as the following:

$$P_{ij} = \begin{cases} 1 & \text{if } j < N/2 \quad \text{(gun side)} \\ -mr_j + 1 & \text{if } j > N/2 \quad \text{(target side),} \end{cases}$$

where r_j is the in-plane distance from the central row of portal image pixels and m was defined as a fourth-order polynomial in Y_{eq}, as given by Berry et al. [34].

The water-equivalent dose at $d_m = 1.5$ cm in a water phantom (PD) in the absence of scattering material in the beam's path can therefore be described as follows:

$$PD_{ij} = \left[(PV_{ij} \cdot g) \otimes^{-1} K_{ij}^{\ we} \right] \cdot U_{ij} \cdot P_{ij}(Y_{eq}) \tag{3.2}$$

where $(PV_{ij} \cdot g) \otimes^{-1} K_{ij}^{\ we}$ is the Wiener deconvolution described in Section 3.1.2. In Figure 3.2, the geometry change that Eq. 3.2 describes is shown.

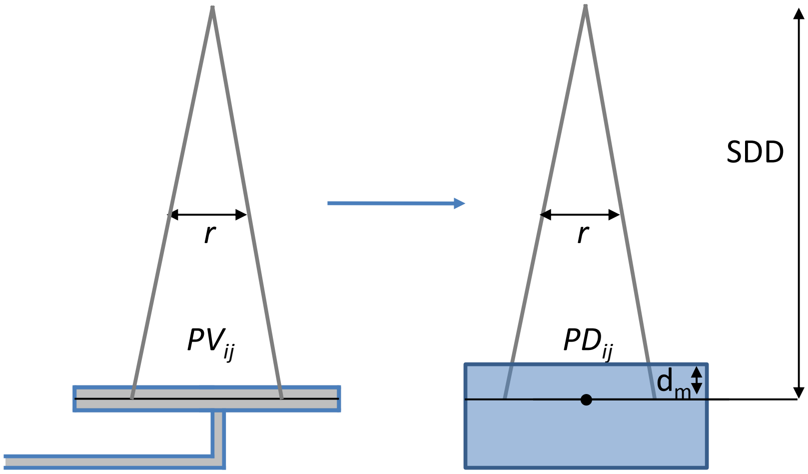

Figure 3.2: Graphical representation of the portal image pixel value (PV) to portal image dose (PD) procedure; $d_m = 1.5$ cm, SSD is the source-to-detector (EPID) distance, and r is the field size at isocenter.

3.2 EPID spectral dependence

Amorphous silicon EPIDs, such as the one used in this study, have been shown to over-respond to low energy photons [63]. Hardening of the primary photon beam (an increase in the beam mean energy) following transmission through a medium (e.g. a phantom or patient) causes a marked decrease in the relative response of the EPID signal compared to corresponding ionization chamber measurements. Ion chambers exhibit a spectral dependence that is closer to water since they are constructed from materials made up of low atomic number materials. Therefore, ion chambers are an excellent choice of standard for dosimetric calibration since they exhibit a minimal beam-quality dependence at therapeutic (MV) photon energies.

In previous transit portal imaging studies, copper build-up plates have been fixed above the EPID in order to reduce the response of the device to low energy photons by attenuating them before they reach the EPID cassette [65]. A copper (or similar material) plate is sufficient to minimize the spectral dependence of the EPID, however, it may introduce patient safety concerns or it may modify the EPID in such a way that is incompatible with the device warranty coverage.

To quantify the difference in response between the EPID and ion chamber dosimeters, Solid Water phantoms (Gammex, Middleton, WI) of varying thickness were mounted at isocenter. A portal imager phantom was set up at 150 cm SDD which consisted of an ion chamber at $d_m = 1.5$ cm in a Solid Water phantom with 5 cm of Solid Water for backscatter. In Figure 3.3, the setup used for these experiments is shown.

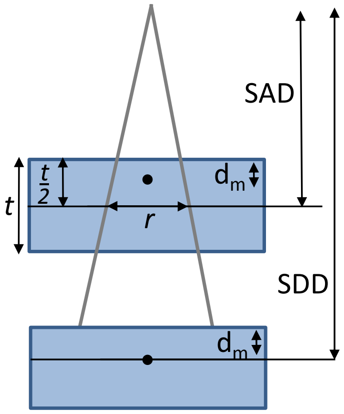

Figure 3.3: Isocentric Solid Water phantom setup to determine beam quality dependence of the EPID. The setup consisted of homogeneous water phantoms of thickness t suspended over a portal imager phantom. SSD is the source-to-detector (EPID) distance, and r is the field size at isocenter.

The ion chamber was used to measure the doses along the beam central axis in the portal image phantom at each phantom thickness, from 5 cm to 30 cm in increments of 5 cm, for three field sizes: 5 × 5 cm^2, 10 × 10 cm^2, and 15 × 15 cm^2. The ion chamber and portal image phantom were removed and replaced with the EPID, and portal images were acquired under the same conditions.

A water-equivalent thickness dependent beam quality correction factor (Q_{ij}) was developed based on the measurements that the above procedure yielded, quantified at each pixel as a function of the scattering thickness (t) above that pixel. The correction factor was defined to be the normalized ratio of ion chamber dose to EPID signal at a point:

$$Q(t) = \left(\frac{\text{Ion Chamber Signal } (t)}{\text{EPID Signal } (t)}\right) \times \left(\frac{\text{EPID Signal } (t=0)}{\text{Ion Chamber Signal } (t=0)}\right)$$

Following the introduction of this spectral correction factor, the water-equivalent dose at d_m in a water phantom at the level of the portal imager ($PD^{\,Tr}$), in the presence of scattering material in the beam's path, can be calculated as:

$$PD_{ij}^{Tr} = PD_{ij} \cdot Q_{ij}(t_{ij}), \tag{3.3}$$

3.3 Patient-to-EPID scatter

Scattered radiation originating in the patient volume can contribute significantly to the portal image signal and is highly dependent on the water-equivalent thickness in the beam's path [66]. An experimental procedure was used to characterize the scatter-to-total dose ratio at the level of the portal imager [67].

In order to estimate the image signal resulting from patient-to-EPID scattered radiation for subsequent removal, a similar procedure as described in Section 3.2 was followed. Solid Water phantoms were mounted at isocenter and the same portal imager phantom was set up at 150 cm SDD. Doses along the beam central axis for three field sizes (5 × 5 cm^2, 10 × 10 cm^2, and 15 × 15 cm^2) were (1) calculated at $d_m = 1.5$ cm in an isocentric mounted water phantom by the TPS and (2) measured by an ion chamber in a portal image phantom for each phantom thickness from 5 to 30 cm in increments of 5 cm.

3.3.1 Pencil beam linear attenuation coefficient

An empirical pencil-beam linear attenuation coefficient was determined by extrapolating: (1) the isocentric water phantom dose measurements to the zero-area phantom dose at d_m (D_m^p) and (2) the portal image phantom dose measurements to the zero-area portal image dose (PD^p). These two primary doses are related according to the equation [67]:

$$PD_m^p = D_m^P \times \exp(-\mu \cdot (t - d_m)) \times \left(\frac{\text{SSD } + d_m}{\text{SDD}}\right)^2 \tag{3.4}$$

where t is the scattering material thickness, μ is the zero-area (pencil-beam) linear attenuation coefficient, SDD is the source-to-detector (portal imager) distance, SSD is the source-to-surface (phantom) distance, and $d_m = 1.5$ cm.

3.3.2 Scatter-to-total dose at the EPID level

The primary dose at the level of the EPID was calculated for each scatterer thickness using the pencil-beam linear attenuation coefficient. The primary dose was compared to the total dose measured using the ion chamber in order to determine the fraction of dose due to scattered radiation from the water phantoms.

In this study, the estimated portal image dose due to scattering radiation was removed by deconvolution with a kernel (K_{ij}^{pt}) that modelled scattering radiation that originated within the patient volume. The patient-to-EPID scatter kernel was developed as a function of the scatterer thickness based on the scatter-to-total dose measurements at the EPID level. The patient-to-EPID scatter kernel was of the form proposed by Spies and Bortfield [68] in their model for a variable point-source mode for multiple scattering events. The kernel,

$$K_{ij}^{pt} = \begin{cases} B_1/(r_{ij}^2 + \beta^2)^{3/2} & \text{if } r_{ij} > 0 \\ B_2 & \text{if } r_{ij} = 0 \end{cases} \tag{3.5}$$

was sufficient to deconvolve the patient-to-EPID scatter and thus calculate the primary dose at the level of the portal imager in the acquired images. The kernel parameters B_1, B_2 and β were characterized for each scattering thickness.

When the transit portal image dose (PD_{ij}^{Tr}) was deconvolved with the patient-to-EPID scatter kernel (K_{ij}^{pt}), the resulting quantity (PD_{ij}^{p}) yielded the dose due to primary radiation at the level of the portal imager:

$$PD_{ij}^{p} = PD_{ij}^{Tr} \otimes^{-1} \left[K_{ij}^{pt}(t_{ij})\right] \tag{3.6}$$

3.4 Backprojection algorithm

The radiological path length of the patient related to each portal image pixel was necessary in order to account for an estimate of the patient-to-EPID scatter described above and attenuation of the radiation beam in heterogeneous media. For dose reconstruction, path lengths can be calculated using a planning CT image set. Reconstruction of VMAT treatments in particular necessitates using the CT image set to calculate beam attenuation [24, 54]. In this study, a relative electron density weighted ray-tracing procedure was performed [69]. The patient planning CT image set was first converted from the units of CT images (Hounsfield Units, HU) to relative electron density (ρ_e) according to data from the BCCA-VIC CT scanner calibration curve. Three linear segments were fitted to the data.

Two radiological path lengths were calculated for each beam. The 'radiological thickness', t_{ij}, was the total water-equivalent thickness of the patient and was used to account for the total attenuation of the beam in reaching the portal imager. The 'radiological depth', d_{ij}, was the water-equivalent depth in the patient to the plane at isocenter normal to the beam central axis of a rayline that intercepted a portal image pixel (i, j). These quantities are illustrated in Figure 3.4.

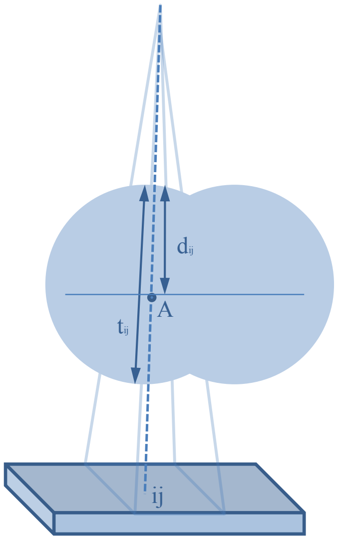

Figure 3.4: Illustration of radiological thickness (t_{ij}) and radiological depth to isocenter (t_{ij}) for a pixel (i, j). 'A' denotes the isocenter, and the plane at isocenter normal to the central axis is shown with a solid horizontal line.

Radiological path lengths for a single rayline (ℓ) were calculated as follows:

$$\ell = \sum_m (\Delta \ell_i) \cdot \rho_{e,m},$$

where the summation m is over the CT image set voxels of a given rayline, $\Delta \ell_m$ is path length through the voxel m of a given rayline, and $\rho_{e,m}$ is the relative electron density of the voxel m.

3.4.1 Transmission to isocenter

The transmission factor that must be applied to the primary dose at the level of the portal imager in order to obtain primary dose at the isocenter plane consists of three components. The attenuation of the primary radiation through the patient must first be accounted for, followed by transportation of the primary radiation through the patient to the plane at isocenter. An inverse-square law factor to account for the beam divergence must also be included. The transmission factor required to back-project the primary dose at the level of the portal imager ($D^{\,p}$) to the isocenter plane in the patient is:

$$T_{ij} = \exp\left(\mu \cdot (t_{ij} - d_{ij})\right),$$

and the primary dose to the plane at isocenter in a patient volume can be calculated as:

$$D_{ij}^{\,p} = PD_{ij}^{\,p} \cdot T_{ij} \cdot \left(\frac{SDD}{SAD}\right)^2 \tag{3.7}$$

3.4.2 Patient scatter

A significant fraction of the patient dose occurs due to scattered radiation originating within the patient volume. The fraction of scattering radiation compared to primary radiation increases with depth and field size. A convolution kernel (K_{ij}) was developed to model of scattered radiation within the patient.

Solid Water phantoms, with thickness ranging 10 cm to 30 cm in increments of 10 cm, were mounted at isocenter and open fields of 5 × 5 cm^2, 10 × 10 cm^2, and 15 × 15 cm^2 were delivered at each thickness. Portal images were acquired for each field and back-projected primary portal image doses were calculated at the isocenter plane in the phantoms. The dose to the isocenter plane was calculated using the TPS for the three field sizes at each thickness under the same geometry. The kernel (K_{ij}) was chosen such that when it was convolved with the back-projected primary dose plane, the convolved total dose planes at isocenter matched the corresponding dose planes from the TPS.

Kernel parameters were calculated for three radiological depths (5 cm, 10 cm, and 15 cm) to characterize the scattering behaviour as a function of depth. The form of the scattering kernel was chosen have a similar form to pencil beam models [40, 41]. The kernel had empirical form shown below:

$$K_{ij}^{\,sc} = E_1 \exp(-\epsilon_1\ r_{ij}) + E_2 \exp(-\epsilon_2\ r_{ij}) + E_3 \exp(-\epsilon_3\ r_{ij}) \tag{3.8}$$

where the coefficients E_1, E_2 and E_2 were fitted for each radiological depth while the attenuation coefficients ϵ_1, ϵ_2 and ϵ_3 were fixed. The parameters were chosen such that the squared difference between TPS dose distributions and convolved portal image isocenter dose distributions were minimized. The kernel coefficients for intermediate scattering thicknesses were interpolated.

The total dose to the isocenter plane (D) in a patient or phantom can be calculated by:

$$D_{ij} = D_{ij}^{\,p} \otimes \left[K_{ij}^{\,sc}(d_{ij}) \right] . \tag{3.9}$$

The above dose, as measured by the portal imager, will be denoted by D_{ij}^{PI} to distinguish it from the corresponding patient dose as calculated by the treatment planning system, D_{ij}^{TPS}.

3.5 Adaptation for VMAT reconstruction

Two-dimensional beam's eye view EPID dosimetry is a well-established IMRT QA technique. However, 2D *in vivo* measurements are not possible with single integrated portal images because off-axis pixels do not correspond to specific locations in the phantom or patient except along the axis of gantry rotation.

3.5.1 Justification of a one-dimensional calculation

In reconstructing the planar dose for IMRT fields, there is a one-to-one correspondence between a point on the EPID and a pixel in the isocenter plane perpendicular to the beam central axis. However, when integrated images are acquired from VMAT beams, the above relationship is generally lost. Since the EPID is continuously rotating about the patient, a general pixel off of the portal image v-axis corresponds to an annulus of dose within the patient from a single rayline, as illustrated in Figure 3.5, and any single dose point on the annulus maps to a line in the $u-$direction on the EPID. The mapping of the signal along the EPID $v-$axis to the dose along the axis of gantry rotation is shown in Figure 3.6. If the analysis is limited to the signal of the portal image $v-$axis ($u = 0$), it can be shown that the signal of this profile maps directly to the dose along the axis of gantry of rotation. Therefore, a one-to-one correspondence exists between a point on the portal imager and a voxel in the patient - an analogous situation to the IMRT back-projection model.

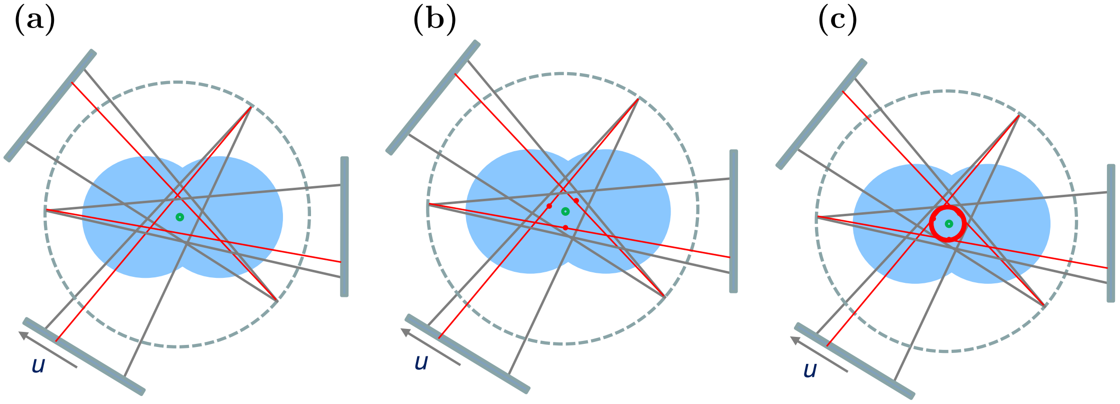

Figure 3.5: Mapping of off-axis pixel to an annulus of patient dose in VMAT verification. **(a)** Consider a single, general off-axis pixel of an integrated portal image during VMAT delivery from a single rayline (red). **(b)** When back-projected to isocenter, the pixel describes **(c)** an annulus of dose in the patient from this rayline.

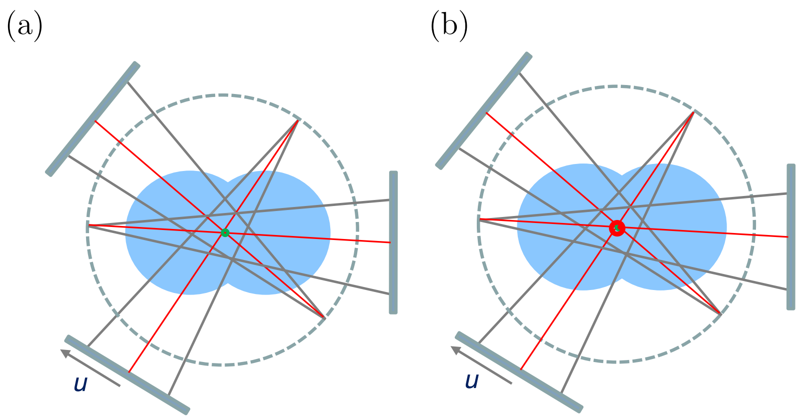

Figure 3.6: Mapping of on-axis pixel to dose at gantry rotation axis in VMAT verification. **(a)** Consider a single, general ON-axis pixel of an integrated portal image during VMAT delivery from a single rayline (red). **(b)** When back-projected to isocenter, the pixel describes the dose along the gantry rotation axis.

Thus, when calculating an *in vivo* dose from a single integrated portal image in VMAT delivery, the approach taken is to treat the integrated arc image as a single static field incident on a rotationally averaged representation of the patient and examine only the dose of the EPID v-axis.

3.5.2 Rotationally averaged transmission factor

In Varian's implementation of VMAT (known as RapidArc®), the beam is controlled by a linear sequence of partial arc segments known as control points. The number of control points is determined in advance by the TPS based upon the user-defined total angle subtended by the treatment arc. For a single 360° arc, 178 control points are encoded in the plan file. Each control point is labelled with a gantry angle and cumulative meterset weight (CMW). The CMW indicates the planned fraction of the beam to be delivered by the time the gantry angle of the control point is reached; the meterset weight (MW) is therefore the fraction of beam delivered during a single control point. Mathematically, the MW is calculated by taking the derivative of the CMW with respect to the control point.

In this study, gantry angles and MWs were binned in segments of five consecutive control points, reducing the control point list size by a factor of five so that there were 36 "new" control points used for calculations. The radiological thickness (t_{ij}) and depth to isocenter (d_{ij}), as defined in Section 3.4, were calculated at the median gantry angle of each control point segment. This procedure yielded 36 thickness (t_{ij}) and depth to isocenter (d_{ij}) matrices at equally spaced intervals of approximately ten degrees. The cumulative transmission factor that can be applied to a single integrated portal image over all new control point segments, k, was therefore calculated as:

$$T_{ij} = \sum_{k=1}^{N} \mathrm{MW}_k \times [\ \exp\left(\mu \cdot (t_{ij,k} - d_{ij,k})\right)\ ]$$

This form of T_{ij} replaces the form of T_{ij} used in Eq. 3.7. The adapted VMAT backprojection technique effectively treated the VMAT arc as a single static field incident upon a virtual, rotationally averaged representation of the patient at isocenter. Due to the symmetry of the rotational averaging, the dose to this virtual patient along the $z-$axis in the plane at isocenter (the dose to the $v-$axis of the portal imager) is the *in vivo* dose to the patient along the axis of gantry rotation. The remainder of the radiation field does not directly represent a physical dose within the patient.

Lateral scatter deconvolution, beam hardening correction, patient-to-EPID scatter deconvolution, and patient scatter convolution were performed as in the procedure for single static fields developed in this section. The coefficients of the kernels and fitted polynomials were calculated as the weighted average (as weighted by the meterset weight) of each coefficient that would be calculated for individual projections.

Chapter 4

Results (I)

This chapter presents the results of the experiments that were performed to characterize the EPID. Calculation and testing of the back-projection algorithm parameters are presented (Sections 4.1–4.4). Initial results of open and modulated fields measured in homogeneous water phantoms using the back-projection are also assessed (Section 4.4).

4.1 EPID dose calibration

4.1.1 Absolute dose calibration

Two Varian aS1000 EPIDs were calibrated in this study since patient measurements were later acquired on two treatment units. Calibration portal images were acquired as described in Section 3.1.1 for each of the two EPIDs. These calibration images provided unique pixel value-to-dose conversions for each EPID. The calibration value represented the only algorithm parameter that varied between the two EPIDs; the remainder of the parameters presented in this section are independent of the EPID used.

The pixel value to dose conversion factor for the first EPID was $g = 1.044$ cGy/CU and for the second EPID was $g = 1.271$ cGy/CU. The conversion factor had different values for the two EPIDs in part due to the different user-defined Calibration Unit factor that was entered into the XI node software.

4.1.2 EPID optical glare and scatter

When normalized to the 10×10 cm^2 field signal, the relative dose factor for the calibrated portal imager along the central axis is considerably lower than corresponding measurements made in a water phantom at a depth of $d_m = 1.5$ cm for field sizes smaller than 10×10 cm^2 . Conversely, the relative portal image signal is greater than corresponding water measurements for field sizes greater than 10×10 cm^2.

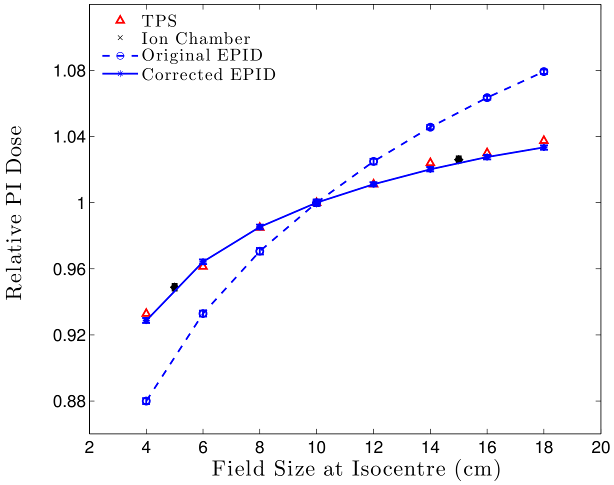

Figure 4.1: Treatment planning system calculated dose ("TPS", red triangles) , ion chamber measured dose ("Ion Ch.", black diamonds), and corrected/deconvolved EPID dose along the central axis ("Corrected EPID", blue closed circles) are shown normalized to the signal of the 10×10 cm^2 field. The uncorrected EPID signal is also shown for comparison ("Original EPID", blue open circles). The error bars are smaller than the data markers.

In Figure 4.1, the relative raw portal image signal and the corrected (deconvolved) portal image signal along the central axis are shown for square fields of 4×4 cm^2 to 18×18 cm^2. The corrected portal image signal closely matches relative dose measurements made in a water phantom at $d_m = 1.5$ cm for all field sizes. The deconvolution procedure was performed as detailed in Section 3.1.2.

The two dimensionless coefficients for the lateral scatter kernel (${K_{ij}}^{we}$), described in Section 3.1.2, were determined by a least-squares optimization to be: $A_1 = 1.75 \times 10^{-5}$cm $\pm\, 0.01 \times 10^{-5}$ cm and $A_2 = 0.89 \pm 0.01$. The attenuation coefficient, $\alpha = 0.09$ cm^{-1}, was fixed during the optimization. The uncertainty in the parameters above represent the increments of the search space during the optimization of the parameters A_1 and A_2. This kernel and its parameters are not unique; there is likely a wide range of acceptable parameter values. The parameters presented here are the results of an two-parameter optimization that was performed with the form of the kernel estimated in advance. Other acceptable parameter combinations may yield comparable accuracy.

The absolute dose difference between corrected portal image relative dose factor along the central axis and the treatment planning system relative dose factor was less than 0.5%. The minimum difference was -0.5% and the greatest dose difference was 0.4%. The largest differences in magnitude between portal image and water measurements were observed to occur with the smallest and largest field sizes.

4.1.3 Additional dosimetry corrections

The linear off-axis correction factor (U_{ij}), described in Section 3.1.3, that was applied to the image matrix was linear in radial distance from the centre pixel where the slope was $u_1 = 0.018$ cm^{-1} and the $y-$intercept was $u_0 = 1.00$. The EPID backscatter correction (P_{ij}) had the coefficients fitted as described in Berry et al. [34], with the modification that the equivalent inferior field length (Y_{eq}) was used in place of the $Y1$ jaw size. The use of the equivalent jaw size was required in this study since the collimator angle was not necessarily zero as in the work of Berry et al. [34].

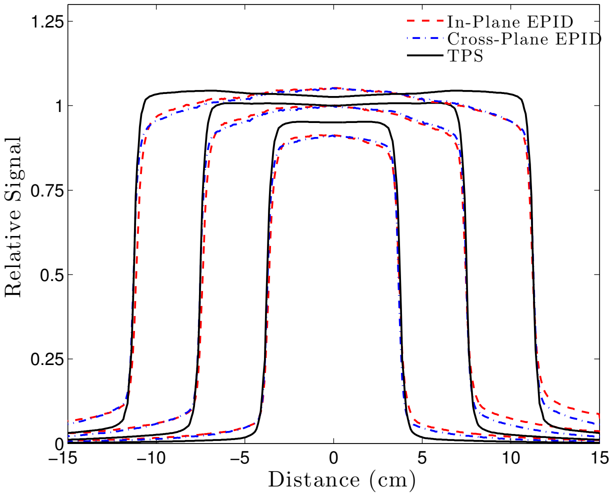

Figure 4.2: Raw in-plane EPID (dashed red line) and cross-plane EPID (dashed-dotted blue line) profiles through 5 × 5 cm^2, 10 × 10 cm^2, and 15 × 15 cm^2 square fields at 150 cm SDD. Measurements were normalized to the 10 × 10 cm^2 signal along the central axis. No material was placed above the EPID. Ideal treatment planning system (TPS, black line) generated profiles are shown for comparison.

In Figure 4.2, uncorrected (raw) portal image signal profiles are shown compared to treatment planning system profiles of the dose to water at $d_m = 1.5$ cm in a water phantom. The non-water equivalent field-size dose dependence, profile rounding due to flood field calibration, and disagreement within the umbra region of the portal image profiles are all apparent in these profiles. Furthermore, the EPID backscatter effect is apparent; the signal of the in-plane profile in the inferior direction (negative distance from the central pixel) has a greater magnitude than corresponding cross-plane measurements.

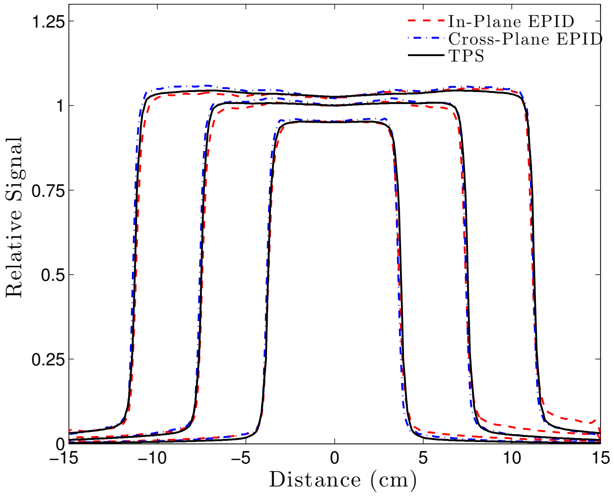

Figure 4.3: Corrected in-plane EPID (dashed red line) and cross-plane EPID profiles (dashed-dotted blue line) through 5 × 5 cm^2, 10 × 10 cm^2, and 15 × 15 cm^2 square fields at 150 cm SDD. Measurements were normalized to the 10 × 10 cm^2 signal along the central axis. No material was placed above the EPID. Ideal treatment planning system ("TPS", solid black line) generated profiles are shown for comparison.

In Figure 4.3, corrected dose profiles of three field sizes—with lateral scatter deconvolution, off-axis correction, and backscatter correction—are shown compared to treatment planning system profiles of the dose to water at $d_m = 1.5$ cm in a water phantom. Following the application of the correction factors described in this section, portal image profiles showed excellent agreement with those that would be measured in a water-equivalent dosimeter. Note that due to the backscattered radiation from the asymmetric construction of the EPID, the portal image signal in the superior in-plane umbra region (positive distance from the central pixel) remained substantially higher compared to the inferior in-plane umbra signal.

4.2 EPID spectral dependence

As discussed in Section 3.2, when the low energy components of the open beam spectrum are attenuated by the a phantom or patient, the portal image signal decreases appreciably. The ratio of EPID to ion chamber signals diverges as the phantom thickness increases. In Figure 4.4(a), the transit portal image and ion chamber signals measured following transmission through homogeneous water phantoms are shown for a 10 × 10 cm^2 field.

The beam quality correction factor (Q_{ij}), described in Section 3.2, was the ratio of the ion chamber measured signal to the portal imager signal (see Eq. 3.2). This correction factor ensured a water-equivalent dose response at the level of the EPID. In Figure 4.4(b), the correction factor for three square field sizes (5 × 5 cm^2, 10 × 10 cm^2, and 15 × 15 cm^2) is shown. The beam hardening correction factor has the lowest magnitude for the largest field size, due to the additional low energy scattered photons that arise from a large collimator opening and field size. For a scattering thickness of approximately 30 cm, the EPID underestimates the dose by approximately 15%. This is a large discrepancy and underlines the importance of a spectral correction.

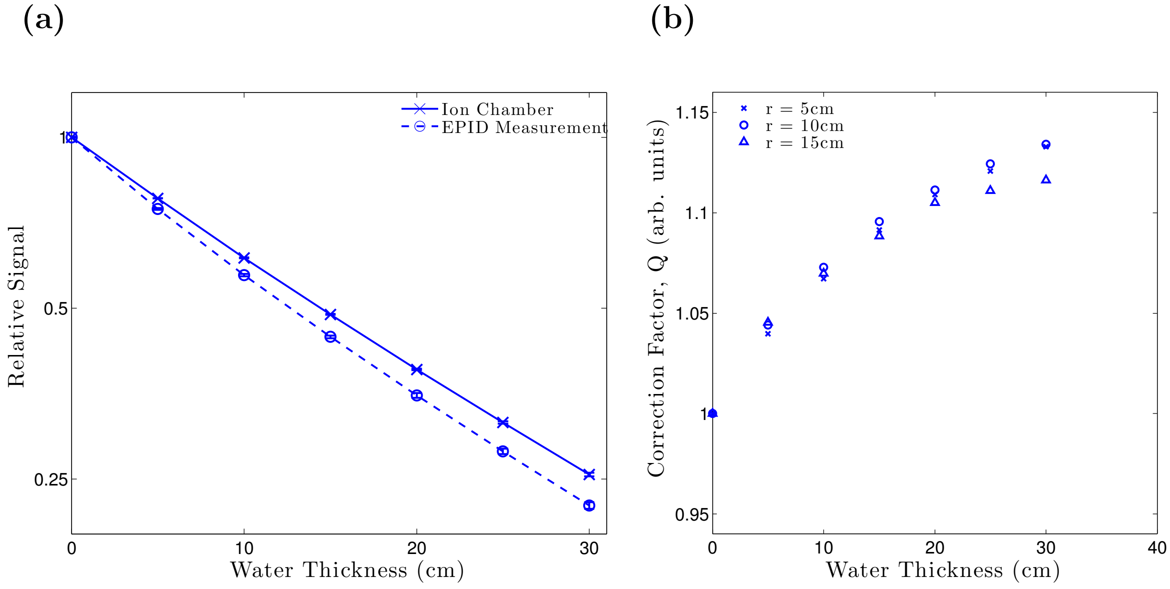

Figure 4.4: **(a)** Relative ion chamber and portal image doses for a 10×10 cm^2 field following transmission through water phantoms. Measurements were normalized to the signal in the absence of a phantom and **(b)** EPID beam quality correction factor, calculated for three field sizes, r. The error bars are smaller than the data markers.

4.3 Patient-to-EPID scatter

In Figure 4.5 the calculation of the 6 MV radiation beam narrow-beam linear attenuation coefficient (μ) is shown. By rearranging Eq. 3.4, the linear attenuation coefficient μ can be solved for graphically by plotting the quantity $\left(-\ln\left[\left(\frac{PD^p}{D^p_m}\right)\left(\frac{SDD}{SSD+d_m}\right)^2\right]\right)$ as a function of $(t-d_m)$. As described in Section 3.3, D^p_m is the extrapolated phantom zero-area dose at d_m, PD^p is the extrapolated portal imager zero-area dose, and t is the homogeneous phantom thickness.

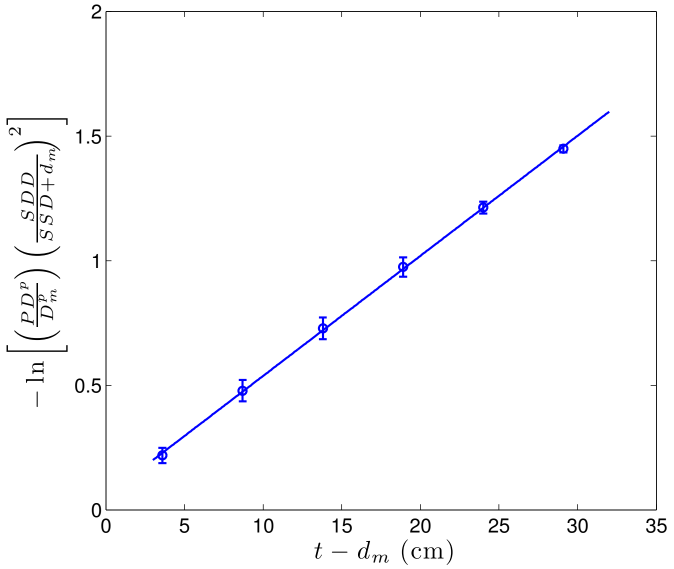

Figure 4.5: Calculation of a pencil beam linear attenuation coefficient using extrapolated zero-area phantom dose (D_P) and zero-area portal image phantom dose (D_{PI}). SAD = 100 cm, SDD = 150 cm, and t is the homogeneous water phantom thickness.

For the 6 MV beam used in this study, it was calculated that the narrow-beam linear attenuation coefficient was $\mu = 0.0482 \pm 0.0005\text{cm}^{-1}$ (slope ± one standard error in the slope). A narrow-beam attenuation coefficient of this magnitude similarly follows from an extrapolation of the broad-beam attenuation coefficients to the zero-area value [14].

In Figure 4.6, the ratio of dose from scatter within the EPID and scatter from the patient to the total dose measured from the portal image is shown. A description of this calculation is detailed in Section 3.3. The fraction of scatter-to-total dose is shown to increase with scattering thickness and with field size; similar dependences were reported by [67].

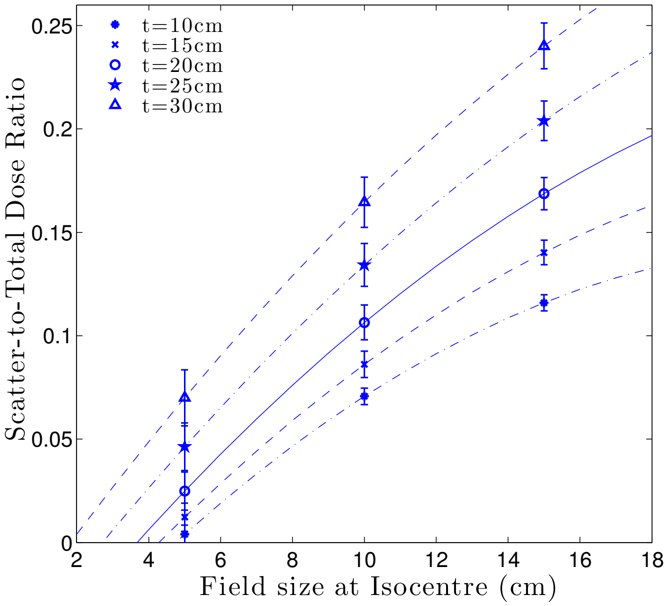

Figure 4.6: Measured EPID scatter-to-total dose ratios plotted as a function of field size for five homogeneous scattering thickness (t). The quadratic curve of best fit is shown with a line for each scattering thickness.

A kernel that modelled scattered radiation from the patient to the EPID (K_{ij}^{pt}) was developed based on the measurements shown in Figure 4.6. In Table 4.1, the best-fit parameters for this scatter kernel are shown. The parameters are as described in Eq. 3.5 and are shown as a function of the three calibration homogeneous water phantom thicknesses. These parameters were observed to follow well defined trends. Intermediate thickness parameters were interpolated from these data; the parameters were extrapolated for thicknesses beyond 30 cm.

Table 4.1: Best-fit parameters for the patient-to EPID scatter kernel (K_{ij}^{pt}, Eq. 3.5) as a function of homogeneous water phantom thickness, t. The uncertainties represent the resolution (increment) used in the parameter optimization.

t (cm)	B_1 ($\times 10^{-3}$ cm^3)	B_2	β (cm)
10	3.5 ± 0.1	1.045 ± 0.05	10.0 ± 0.1
20	4.4 ± 0.1	1.060 ± 0.05	9.6 ± 0.1
30	5.3 ± 0.1	1.070 ± 0.05	9.2 ± 0.1

When patient-to-EPID scatter was deconvolved from portal images following transmission through a *non*-homogeneous phantom, the mean water-equivalent thickness in the beam complete irradiated area outline (CIAO) was used to estimate the required kernel parameters (namely, the parameter t in Table 4.1). The CIAO was defined as those pixels that had a signal greater than 10% of the maximum portal image signal.

As an example, profiles that result from deconvolution with the patient-to-EPID scatter kernel are shown in Figure 4.7. These profiles - representative of primary dose - show the removal of patient-to-EPID scattered radiation and scattered radiation within the EPID that is present in portal images.

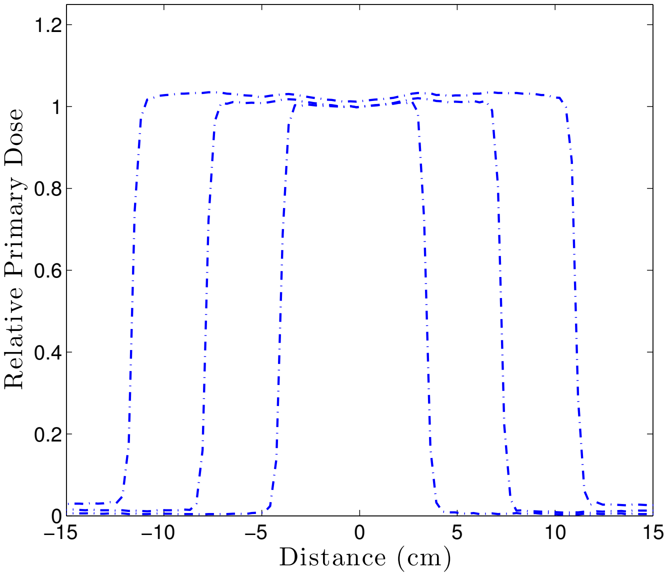

Figure 4.7: Profiles of primary dose to portal imager for three field sizes following deconvolution of the transit portal dose with the patient-to-EPID scatter kernel: 5 × 5 cm^2, 10 × 10 cm^2, and 15 × 15 cm^2 following transmission through a 20 cm homogeneous water phantom. Measurements were normalized to the signal along the central axis of the 10 × 10 cm^2 field and are shown for the cross-plane direction.

4.4 Back-projection algorithm

With the measured value of primary dose at the level of the portal imager, a method for modelling the transportation of this dose to the plane at isocenter was developed. The transportation, or back-projection, consisted of first calculating the transmission (or attenuation) to isocenter, followed by a convolution to simulate scattering radiation within the patient.

4.4.1 Transmission to isocenter

In Figure 4.8, the conversion curve from planning CT number (in Hounsfield Units, HU) to electron density relative to water is shown. This conversion curve was used to convert the planning CT image set into a matrix of voxels with values of electron density relative to water in order to calculate water-equivalent depths within the patient as discussed in Section 3.4.

For low Hounsfield Units (HU $<$ 100, soft tissue), the conversion curve used in this study was approximately linear in HU with a slope 0.001 and $y-$intercept of 0. For high Hounsfield Units (HU $>$ 100), the slope of the conversion curve decreases relative to the slope for low HU.

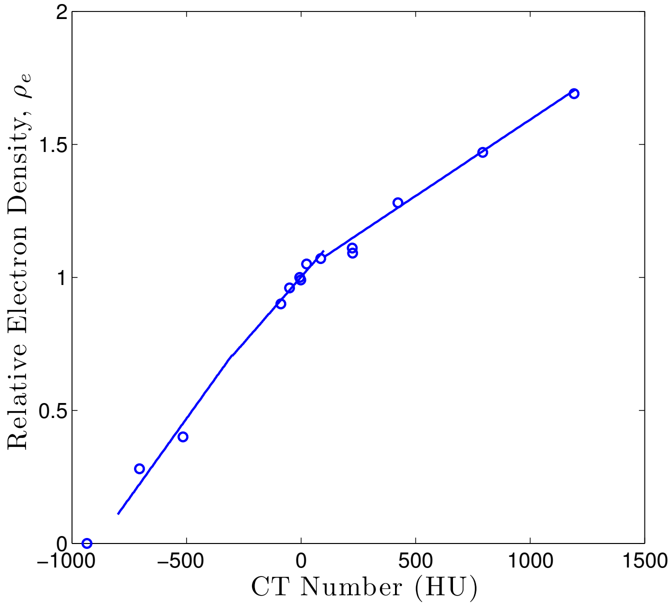

Figure 4.8: Hounsfield unit to relative electron density conversion curve. Institutional scanner calibration data is shown using circular markers; piece-wise linear fit used in this back-projection algorithm is shown using a solid line.

4.4.2 Patient scatter

The attenuation coefficients for the patient scatter kernel (K_{ij}^{sc}), discussed in Section 3.3, were fixed as follows: $\epsilon_1 = 10.0$ cm^{-1}, $\epsilon_2 = 0.50$ cm^{-1}, and $\epsilon_3 = 0.09$ cm^{-1}. The constants were determined by a least-squares optimization for three water-equivalent depths, d, are presented in Table 4.2. Again, the uncertainties on each coefficient represents the increment by which the parameter search space was changed at each step of the optimization. Kernel coefficients for intermediate depths were interpolated and coefficients for depths greater than 15 cm were extrapolated based on the data shown in the table.

Table 4.2: Best-fit parameters for the patient scatter kernel (K_{ij}^{sc}, Eq. 3.8) as a function of homogeneous water phantom depth to isocenter, d. The uncertainties represent the resolution (increment) used in the parameter optimization.

d (cm)	E_1	E_2 ($\times 10^{-5}$)	E_3 ($\times 10^{-6}$)
5	0.106 ± 0.001	5.5 ± 0.1	2.2 ± 0.1
10	0.104 ± 0.001	8.0 ± 0.1	3.1 ± 0.1
15	0.102 ± 0.001	9.5 ± 0.1	3.6 ± 0.1

4.4.3 Reconstruction in homogeneous phantoms

Square fields

In Table 4.3, γ-evaluation pass rates for a global dose difference criterion of 3% and distance-to-agreement criterion of 3 mm at isocenter, are shown for three fields reconstructed at the isocentric plane in homogeneous water phantoms. All fields for all phantom thicknesses tested had γ-evaluation pass rates of greater than 90%, demonstrating strong agreement with treatment planning system dose calculations. The comparison was limited to the CIAO (those pixels with dose greater than 10% of maximum field dose). Agreement within the umbra region appears to diminish with increasing field-size, however, the field edge remains well defined. If the analysis is limited to a high dose area such as the CIAO, discrepancies within the umbra region should not prove problematic. Figure 4.9 shows back-projected profiles in the cross- and in-plane directions for square field sizes of 5×5 cm^2, 10×10 cm^2, and 15×15 cm^2 at a depth of $d = 10$ cm in a $t = 20$ cm homogeneous water phantom.

Table 4.3: Open field γ-evaluation pass-rates ($P_{\gamma<1}$, 3mm/3% global dose difference criteria) as a function of homogeneous water phantom thickness, t.

d (cm)	t (cm)	$P_{\gamma<1}$ (5×5 cm^2)	$P_{\gamma<1}$ (10×10 cm^2)	$P_{\gamma<1}$ (15×15 cm^2)
5	10	94.0%	96.5%	96.5%
10	20	94.5%	96.8%	94.8%
15	30	96.3%	98.1%	98.7%

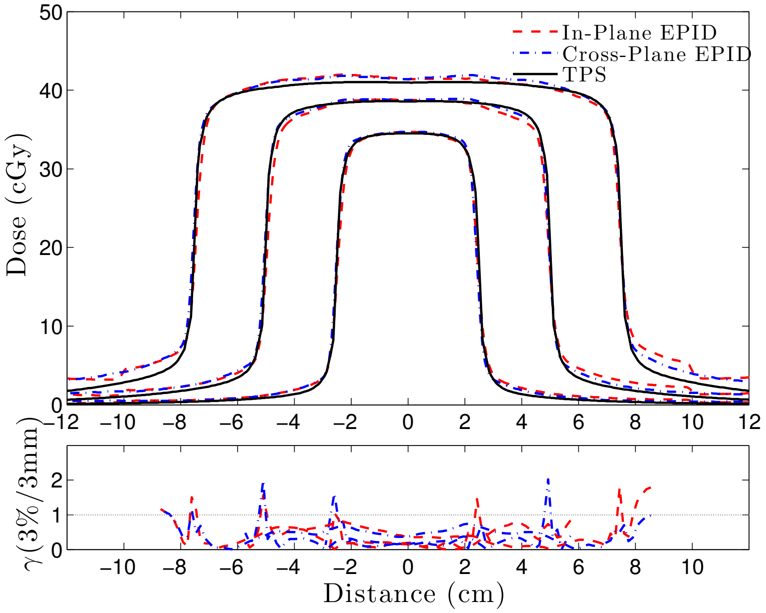

Figure 4.9: Profiles of reconstructed square fields at a depth of $d = 10$ cm in a $t = 20$ cm homogeneous water phantom. In-plane measurements are shown with a dashed red line; cross-plane measurements are shown with a dashed-dotted blue line; TPS calculations are shown with a solid black line. Note that the vertical scale of the upper panel is in units of absolute dose (cGy) and the γ-evaluation criteria was 3%, 3mm.

Modulated fields

Five intensity modulated fields were exported from a patient treatment plan and delivered to a homogeneous water phantom. In Figure 4.10, back-projected profiles of two of the five modulated fields are shown. The profiles show excellent agreement with planned doses. Two-dimensional γ-evaluation pass rates were calculated for these five fields, and 96.9%, 99.2%, 100%, 99.7% and 98.4% of pixels passed the 3%/3mm γ-evaluation within the CIAO.

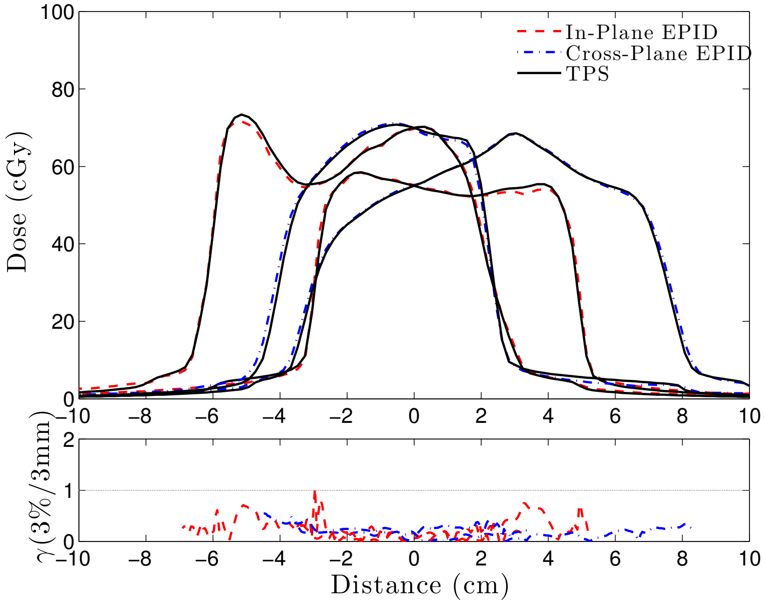

Figure 4.10: Profiles of reconstructed modulated fields at a depth of $d = 10$ cm in a $t = 20$ cm homogeneous water phantom. In-plane measurements are shown with a dashed red line; cross-plane measurements are shown with a dashed-dotted blue line; TPS calculations are shown with a solid black line. Note that the vertical scale of the upper panel is in units of absolute dose (cGy) and the γ-evaluation criteria was 3%, 3mm.

Chapter 5

Results (II)

This chapter presents the results of a clinical study that was undertaken to validate the EPID back-projection techniques (for IMRT and VMAT treatments) developed in this thesis.

Prior to obtaining human participant measurements, the back-projection techniques were tested on an anthropomorphic phantom (Alderson Rando, Radiology Support Devices, Long Beach CA). These phantom measurements are summarized in Appendix A and are compared against patient measurements in Chapter 6.

An IMRT dosimetry study with ten participants and a smaller VMAT dosimetry study with three participants are presented in Sections 5.1 and 5.2 respectively. Since VMAT was only recently implemented at the BCCA-VIC (March 2013), only a small sample of clinical data is able to be presented for this radiotherapy technique.

All of the results presented compare the back-projection techniques to treatment planning system calculations. The dose calculation system used was AAA (v10.0.28, Varian Medical Systems Inc., Palo Alto, CA), the accuracy of which is detailed in Section 2.3.

5.1 Clinical IMRT *in vivo* dosimetry

Ten patients undergoing intensity modulated radiation therapy (IMRT) at the BCCA-VIC were selected to participate in University of British Columbia/BC Cancer Agency Research Ethics Board approved study (approval number H12-02971). The participants were selected by attending radiation therapists at the time of the first treatment based on participant willingness and competency as well as staff timing constraints. The purpose of the study was to validate the back-projection technique on a patient data set and to determine whether the technique is clinically feasible. Data obtained was only used to test the reconstruction techniques and was not used to impact clinical decisions.

The addition of the portal imaging template necessitated extension of each treatment by approximately eight seconds per field. In the Varian TrueBeam implementation, field automation (automatically moving to the next gantry angle with the beam hold on) is not compatible with portal image acquisition. The eight seconds per field were required to manually mode-up the beam again. The participant treatments were otherwise not affected by the inclusion of portal imaging at the time of treatment.

In Table 5.1, the treatment site, fractionation scheme, and number of fractions imaged for each participant is shown. A diverse range of treatment sites were chosen in order to examine the reconstruction robustness.

Table 5.1: Institutional study breakdown of treatment site, number of fields, and fractions imaged for IMRT *in vivo* dosimetry.

Subject ID	Treatment Site	Prescription Dose (Fractions)	# of Treatment Fields	# of Fractions Imaged
H1	Base of Tongue	6000 cGy (30)	5	9
P1	Prostate	7400 cGy (37)	5	9
P2	Prostate	6600 cGy (33)	5	8
C1	Right Brain	6000 cGy (30)	6	8
H2	Base of tongue	6000 cGy (25)	7	8
C2	Right Brain	6000 cGy (30)	6	7
H3	Oropharynx	6000 cGy (25)	7	8
H4	Larynx	6000 cGy (25)	7	7
H5	Right Parotid	3500 cGy (10)	5	5
C3	Right Brain	5600 cGy (21)	6	9
		Totals:	59	78

Portal images were scheduled to be acquired at the first three fractions and every fifth fraction thereafter (approximately once per week). Due to clinical circumstances, the scheduled imaging scheme was not always possible. If a scheduled imaging fraction was missed, the imaging was performed the next possible fraction.

The EPID was set to a source-to-detector distance (SDD) of 150 cm for all image acquisitions and a collision check was performed to ensure that adequate clearance was available between the EPID and the participant.

Before each fraction, orthogonal kV radiographs were obtained with the subject on the treatment bed. These images were compared to planning digitally reconstructed radiographs (DRRs) to determine whether further positional adjustments had to be made before treatment. This is a standardized procedure on TrueBeam units at the BCCA-VIC in order to minimize subject malpositioning ahead of treatment.

In total, 59 unique radiation fields were imaged over 78 fractions. The total data set was composed of 460 portal images, 174 of which were from the participants' first three fractions. Out of the ten study participants, one was excluded from the analysis since this subject had bolus applied to the skin during treatment that was not recorded in the initial CT scan (Subject ID: H5). Bolus is a water-equivalent material that is used to reduce the effective depth of maximum dose in the subject, d_m, in order to eliminate the build-up effect that occurs at depths of less than $d_m = 1.5$ cm. Since the back-projection relies on measurements made with the planning CT data set, bolus can not yet accurately be modelled by the reconstruction technique. However, if the bolus thickness is known for each field, it may be possible to add the water-equivalent thickness to the radiological thickness and depth matrices as a constant offset.

In Figure 5.1, multiple stages of the reconstruction process for a clinical prostate treatment field are shown. Figure 5.1(a) demonstrates a profile through the portal image $v-$axis showing the raw portal image signal. The corresponding portal image dose and primary portal image dose are shown in Figure 5.1(b). For this field, the radiological thickness of the subject and depth to isocenter of the field, shown in Figure 5.1(c), are approximately constant at 20 cm and 10 cm respectively. The reconstructed dose distribution, following back-projection using a calculated transmission factor and phantom scatter convolution, shows excellent agreement with the treatment planning system calculated dose as shown in Figure 5.1(d).

In Figure 5.2, the same stages of the reconstruction process that were shown for the prostate case are shown for a considerably more complex head and neck treatment field. The treatment field is highly modulated as shown in Figure 5.2(a) and the subject anatomy in this region is much more complex as indicated in Figure 5.2(c). Nevertheless, the reconstructed dose distribution shows good agreement with the TPS dose, shown in Figure 5.2(d).

Figure 5.3 shows example output from the reconstruction software. For the purposes of qualitative user evaluation, the treatment planning system dose plane perpendicular to the central axis at isocenter is shown compared to the corresponding reconstructed dose plane. The array of statistics comparing the two dose distributions is displayed together with two-dimensional dose-differences and γ-evaluations.

Prostate field (P1, GA 0°, Fx 34):

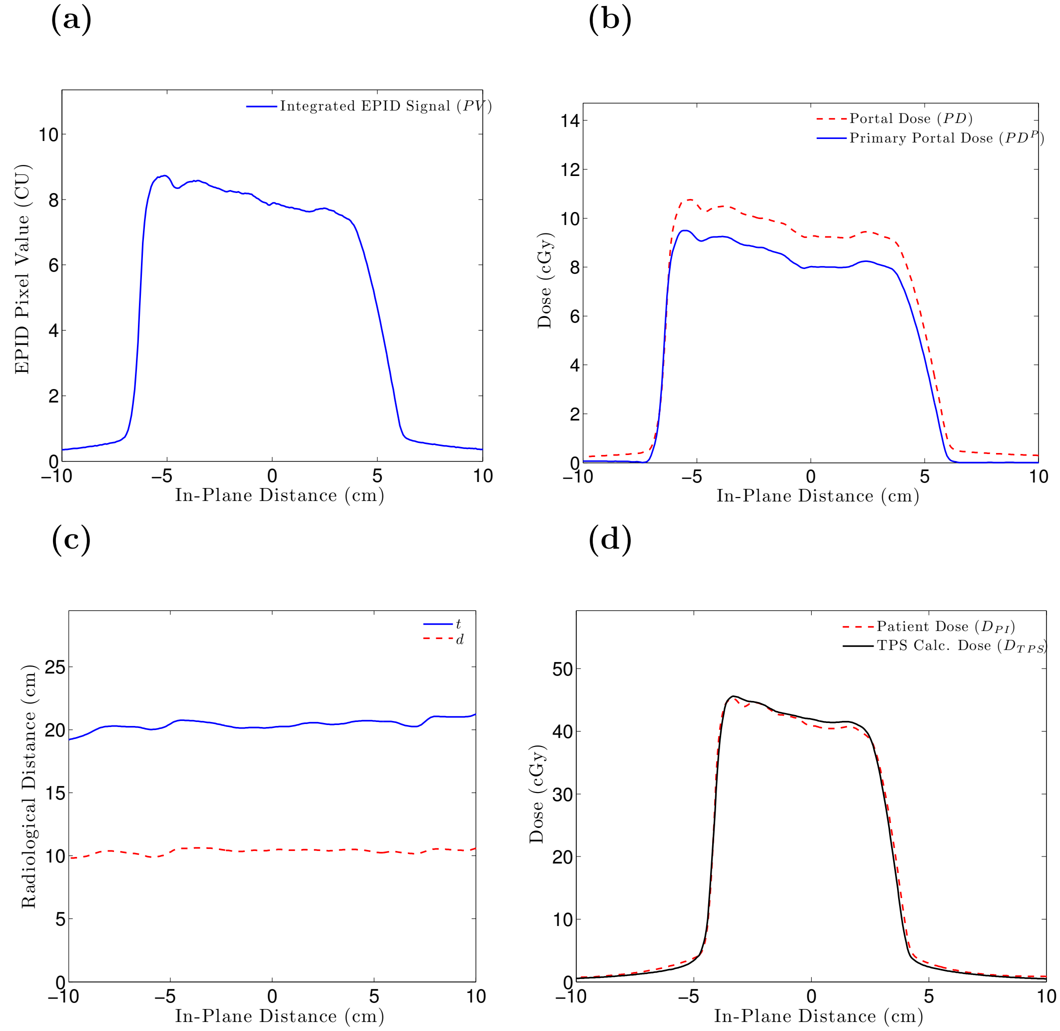

Figure 5.1: Clinical prostate treatment field reconstruction showing: **(a)** Raw portal image signal along the $v-$axis **(b)** Portal dose following dose calibration procedure described in Section 3.1.1 and primary portal dose following patient-to-EPID scatter removal **(c)** Radiological thickness (denoted by label 't') and depth ('d') profiles calculated from the subject's CT data set **(d)** Final *in vivo* dose following back-projection and patient scatter convolution.

Head and neck field (H3, GA 285°, Fx 21):

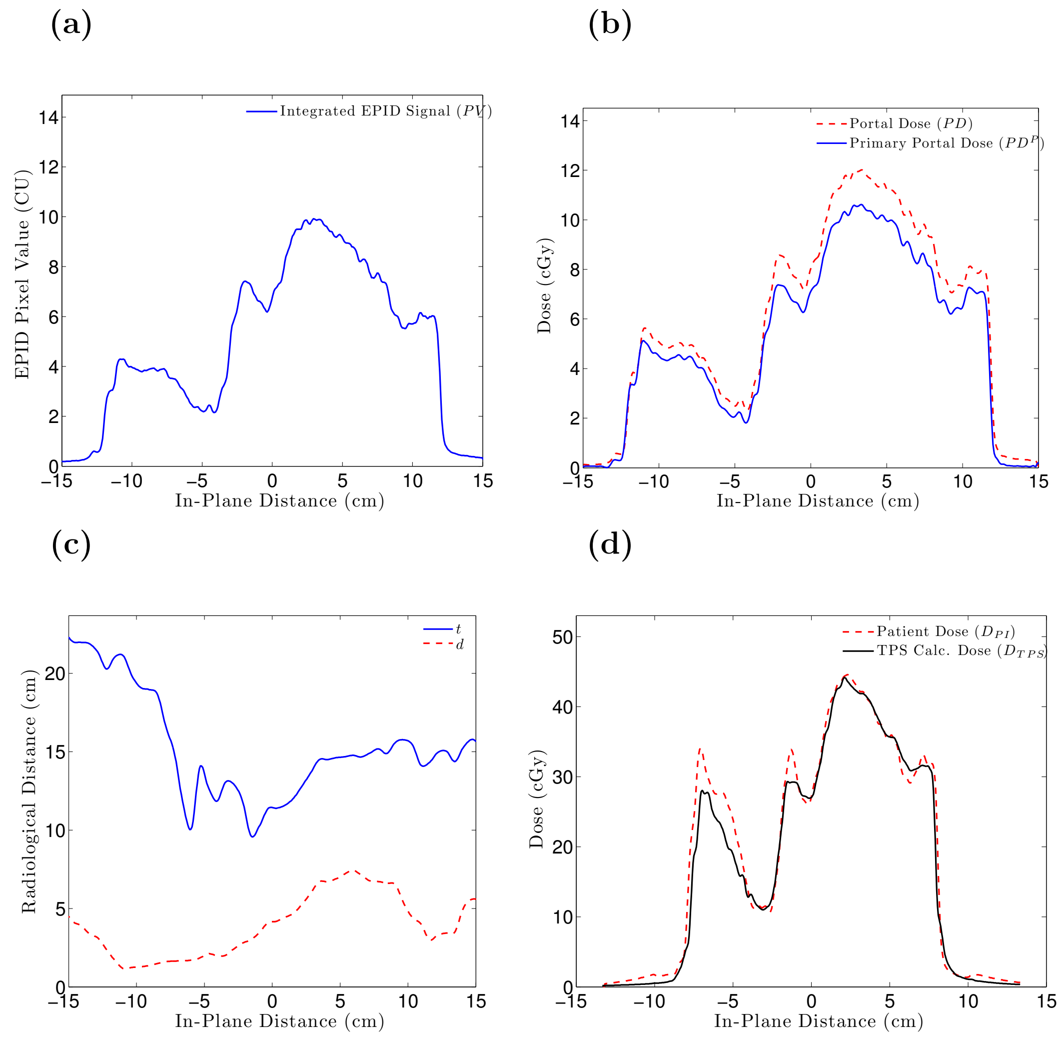

Figure 5.2: Clinical head and neck field treatment reconstruction showing: **(a)** Raw portal image signal **(b)** Portal dose following dose calibration procedure described in Section 3.1.1 and primary portal dose following patient-to-EPID scatter removal **(c)** Radiological thickness (denoted by label 't') and depth ('d') profiles calculated from the subject's CT data set **(d)** Final *in vivo* dose following back-projection and patient scatter convolution.

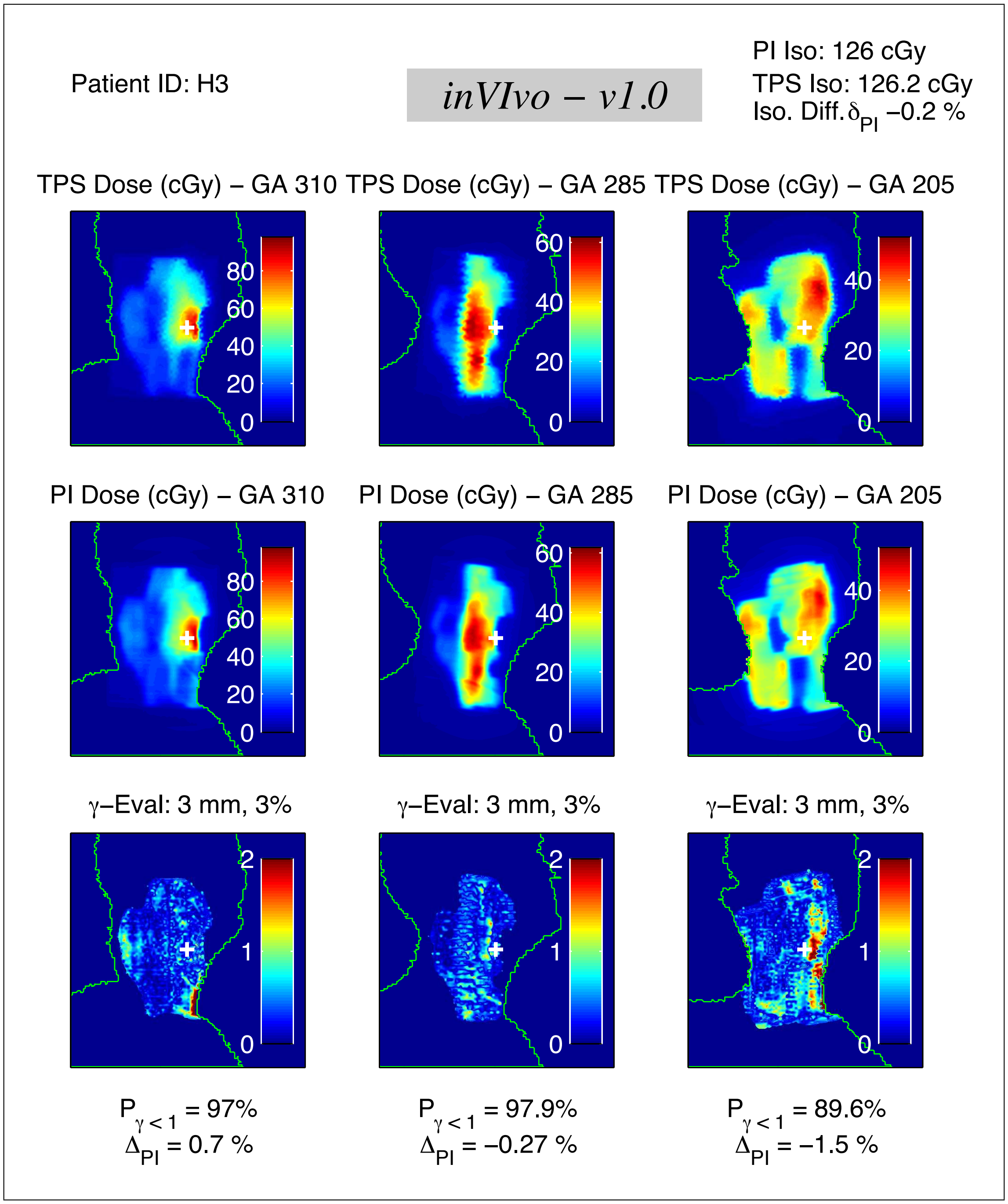

Figure 5.3: Example output from the EPID dose back-projection program. The fields are labelled by their respective gantry angle (GA); the isocenter is denoted by a white cross.

5.1.1 Dose at isocenter (0D)

The first three portal image sets acquired from each participant in the study were verified by the back-projection technique. Results were aggregated only for the first three fractions so as to exclude possible systematic deviations that occur over the course of a treatment (e.g. weight loss) in the initial accuracy evaluation.

The point dose at isocenter from back-projected portal images (D_{iso}^{PI}) was calculated by averaging a 5 × 5 pixel (2.6 mm × 2.6 mm) region along the central axis of the portal image-generated dose plane. This averaging was done in order to facilitate comparison with the treatment planning system which had a comparable dose voxel size (2.5 mm × 2.5 mm × 2.5 mm). The portal image dose at isocenter was compared to the corresponding planned isocenter dose (D_{iso}^{TPS}), and the isocenter dose difference (δ_{PI}) was calculated as:

$$\delta_{PI} = \frac{D_{iso}^{PI} - D_{iso}^{TPS}}{D_{iso}^{TPS}} \tag{5.1}$$

In Figure 5.4, a frequency histogram of the total (sum of all fields) isocenter point dose difference for each fraction is shown.

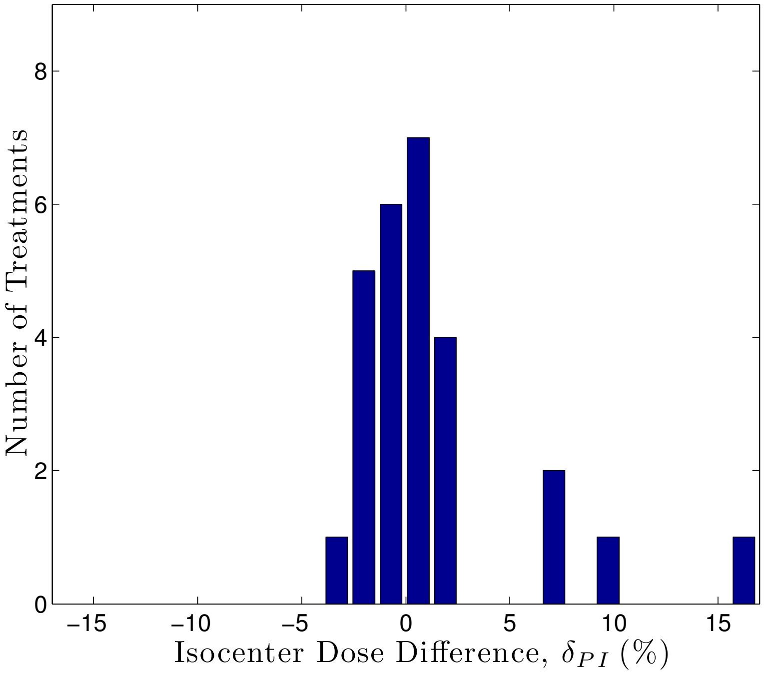

Figure 5.4: Frequency histogram of the isocenter point dose differences of the $n = 27$ fractions (summed isocenter doses of all fields for the first three fractions of each treatment imaged in the clinical validation study).

Reconstructed *in vivo* isocenter point doses in Figure 5.4 had a mean difference of $\overline{\delta_{PI}} = 0.0\%$ (with standard deviation of the differences $\sigma_{\delta_{PI}} = 4.3\%$) when compared to treatment planning system isocenter point doses ($n = 27$ clinical treatments verified). The minimum isocenter dose difference was $\delta_{PI} = -4.4\%$ and the maximum isocenter dose difference was $\delta_{PI} = 15.3\%$.

Reconstructed portal image isocenter doses were in good agreement with planned isocenter doses. The largest discrepancies between the portal image back-projected dose and the TPS dose (those with a point dose difference of greater than five percent) are discussed in Chapter 6.

5.1.2 Dose at axis of gantry rotation (1D)

In Figure 5.5, the dose along the axis of gantry rotation is plotted for two total treatment reconstructions. Figure 5.5(a) shows the sum of five profiles from the five prostate cancer treatment fields of subject P1. Figure 5.5(b) shows the sum of seven profiles from the seven head and neck cancer treatment fields of subject H3.

Minimal quantitative evaluations of these dose profiles are presented; these results are shown only for analogy with VMAT dose profiles along the axis of gantry rotation.

5.1.3 Dose at isocentric plane (2D)

To qualitatively evaluate the complete two-dimensional dose plane that is reconstructed during the IMRT *in vivo* back-projection, two evaluation metrics were employed. The mean dose difference across the plane and a two-dimensional γ-evaluation were used to assess reconstruction accuracy in two dimensions. Again, only the first three fractions of each subject's treatment were verified.

Mean dose difference

The relative dose difference matrix (δD_{ij}) was defined as:

$$\delta D_{ij} = \frac{D_{ij}^{PI} - D_{ij}^{TPS}}{D_{max}^{TPS}}$$

where D_{ij}^{PI} is the back-projected *in vivo* dose plane and D_{ij}^{TPS} is the corresponding dose plane calculated by the treatment planning system (TPS). The dose difference was normalized to the maximum dose of the TPS dose plane (D_{max}^{TPS}). The mean dose difference of a field (the two-dimensional mean of δD_{ij}) was calculated for those pixels

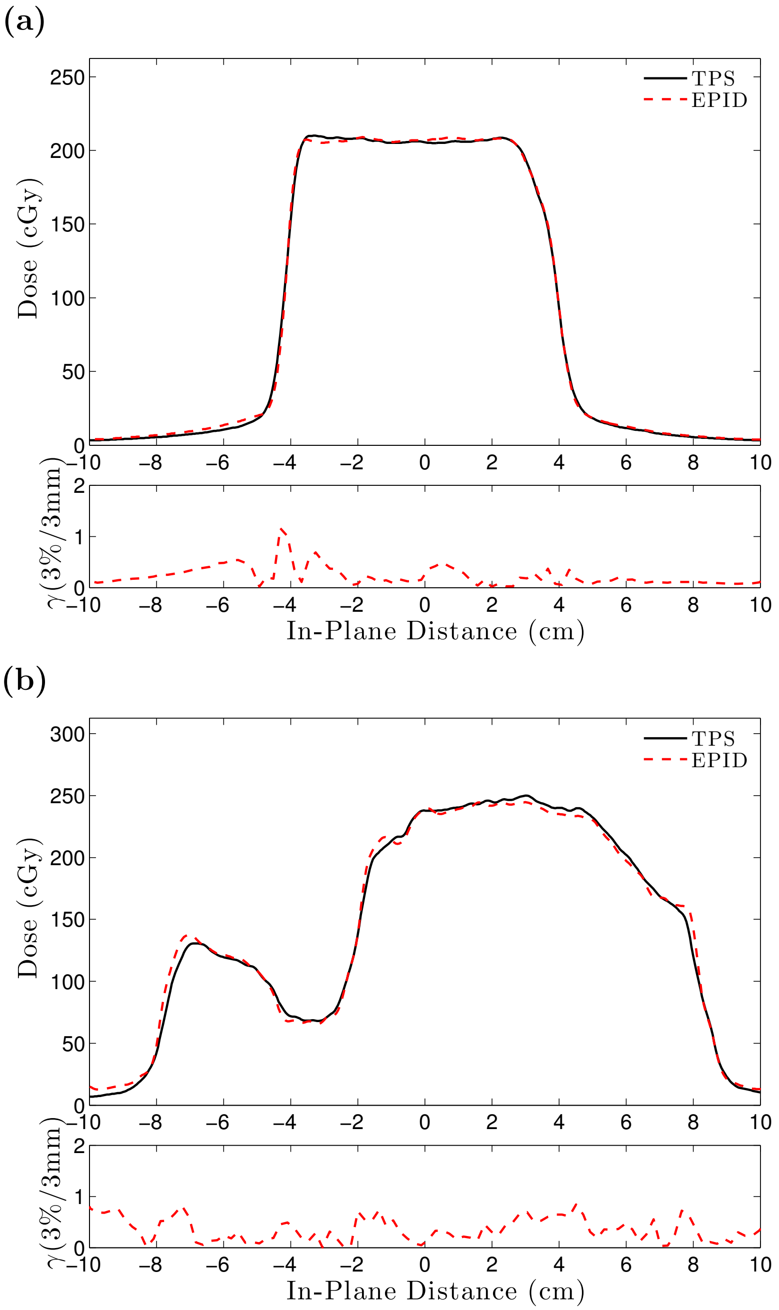

Figure 5.5: Dose along the axis of gantry rotation from IMRT *in vivo* back-projected dose ("EPID", dashed red line) compared to TPS calculations ("TPS", solid black line) for **(a)** a representative prostate treatment case (P1, Fx 29) and **(b)** a representative head and neck treatment case (H3, Fx 3). The inferior direction is towards the negative $x-$axis; the superior direction is towards the positive $x-$axis

with greater than 10% of the maximum dose. If M pixels of a field have greater than 10% of the maximum dose, the mean dose difference of a plane (Δ_{PI}) is calculated as:

$$\Delta_{PI} = \frac{1}{M} \sum_{<i,j>}^{M} \delta D_{ij}$$

In Figure 5.6, a frequency histogram of the mean dose difference is shown. Of the 159 fields that were reconstructed at the isocenter plane in Figure 5.6, the mean dose difference was calculated to be $\overline{\Delta_{PI}}$ = -0.2% (with standard deviation of the differences $\sigma_{\Delta_{PI}} = 2.0\%$). The minimum field mean dose difference was Δ_{PI} = -4.0% and the maximum field mean dose difference was $\Delta_{PI} = 7.4\%$.

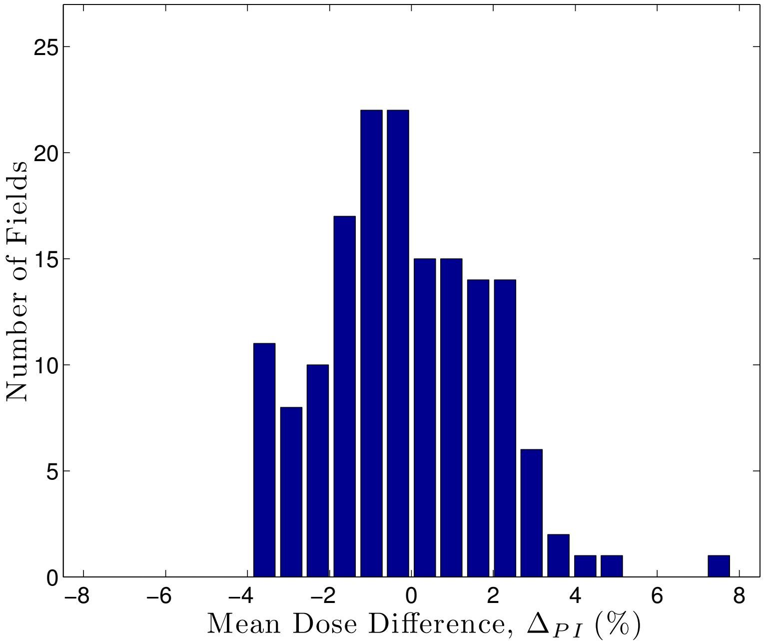

Figure 5.6: Frequency histogram of the mean dose difference of the $n = 159$ fields (first three fractions of each treatment imaged in the clinical validation study).

γ-Evaluation

The γ-evaluation method is described in Section 2.3.2. The γ-evaluation was calculated at each pixel with greater than 10% of the maximum planned dose. The percentage of pixels with a passing γ-evaluation value was reported for each field. The "pass-rate", that is to say a γ-value of less than unity, is denoted by $P_{\gamma<1}$.

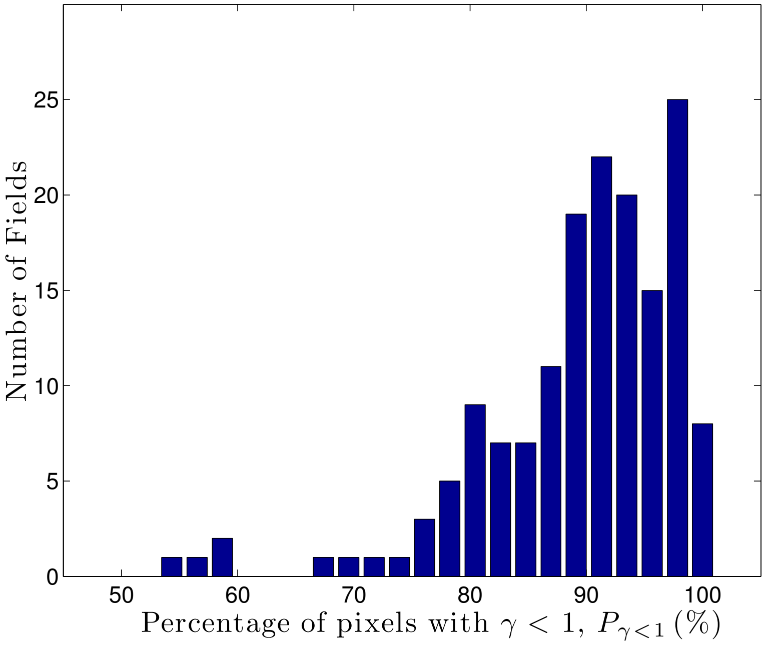

Figure 5.7: Frequency histogram of the γ-evaluation pass-rates of the $n = 159$ fields.

Figure 5.7 shows the frequency distribution of the $\gamma-$evaluation pass rates across all fields examined. Of the 159 fields over the first three fractions that were reconstructed, the mean of the γ-evaluation pass rates was calculated to be $\overline{P_{\gamma<1}} = 89.6\%$ (standard deviation of the pass-rates $\sigma_{P_{\gamma<1}} = 8.6\%$).[1]

The minimum γ-evaluation pass-rate was $P_{\gamma<1} = 53.8\%$ and the maximum was $P_{\gamma<1} = 99.7\%$.

---

[1] In the case of a one-tailed distribution, such as the γ-evaluation pass rate, the standard deviation does not provide a complete description of the data spread. In this case, a method of summarizing the spread of the distribution is to calculate the **95% prediction interval**, the range of the distribution in which 95% of future observations would be expected to fall. The lower limit of the 95% prediction interval is given by $\overline{X} - T_a s_n \sqrt{1 + (1/n)}$, where $\overline{X}$ is the sample mean, n is the sample size, T_a is the 95th percentile of a one-sided Student's t-distribution with $n - 1$ degrees of freedom, and s_n is the sample standard deviation.

In this instance, the lower limit of the 95% prediction interval is $P_{\gamma<1} = 75.3\%$.

5.2 Clinical VMAT *in vivo* dosimetry

The first three patients undergoing volumetric modulated arc therapy (VMAT) at the BCCA-VIC were selected to have integrated portal images acquired during three fractions at the beginning of treatment. Unlike the IMRT *in vivo* measurements of Section 5.1, the addition of the portal imaging template did not lengthen the treatment time since only one arc was employed for all treatments.

The EPID was positioned at 150 cm or 160 cm SDD by the radiation therapists and single integrated portal images were acquired. The radiation fields recorded on the EPID were back-projected and the dose along the axis of gantry rotation was calculated as described in Section 3.5.

In Table 5.2, the treatment site, fractionation scheme, and number of fractions imaged for each participant is shown. Only prostate cancer treatments were imaged since VMAT has only been implemented for treatments of this site at the BCCA-VIC.

Table 5.2: Institutional study breakdown of treatment site, number of fields, and fractions imaged for VMAT *in vivo* dosimetry.

Subject ID	Treatment Site	Prescription Dose (Fractions)	# of Treatment Arcs	# of Fractions Imaged
vP1	Prostate	6600 cGy (33)	1	3
vP2	Prostate	7400 cGy (37)	1	3
vP3	Prostate	7400 cGy (37)	1	3
		Totals:	3	9

5.2.1 Dose at isocenter (0D)

Doses at isocenter from back-projected portal images were calculated by averaging the dose over a five pixel region (2.6 mm) at $z = 0$ of the dose profile along the gantry rotation axis. This averaging was performed in order to facilitate comparison with the treatment planning system, which had a comparable dose voxel size. The PI and TPS isocenter dose differences for each VMAT treatment are listed in Table 5.3.

The mean of the isocenter point dose differences was $\overline{\delta_{PI}} = 1.1\%$ (standard deviation of the differences $\sigma_{\delta_{PI}} = 1.7\%$) among the nine fractions that were analyzed.

Table 5.3: Summary of *in vivo* dosimetry quantities for the VMAT clinical sample.

Subject ID	Fraction #	Isocenter Point Difference δ_{PI} (%)	Mean Profile Difference Δ_{PI} (%)	$\gamma-$Evaluation Pass Rate $P_{\gamma<1}$ (%)
vP1	4	-0.1	-1.5	100
	5	-0.5	-2.0	97.6
	9	-0.3	-1.0	100
vP2	3	4.1	2.2	76.3
	4	3.2	1.4	86.6
	5	2.6	0.4	98.9
vP3	1	0.4	0.0	100
	2	0.3	0.3	100
	3	0.5	0.3	100
	Mean ± 1 SD:	1.1 ± 1.7%	0.0 ± 1.3%	95.5 ± 8.4%

5.2.2 Dose at axis of gantry rotation (1D)

The dose along the axis of gantry rotation in the subject volume is of interest in the VMAT treatment *in vivo* dose reconstruction that has been developed. One dimension is the highest dimension of physical dose that can be extracted from single integrated electronic portal images. The dose reconstruction was first performed in two dimensions using the complete portal image, then the dose along the axis of gantry rotation (the central profile) was extracted from the image.

Dose profiles for the VMAT plans were calculated as a function of distance along the axis of gantry rotation. A one-dimensional mean dose difference was calculated in an analogous manner to the two dimensional case, described by Eq. 5.1.3. The mean dose difference was $\overline{\Delta_{PI}}$ = 0.0% (standard deviation of the differences $\sigma_{\Delta_{PI}}$ = 1.3%). A one-dimensional γ-evaluation was performed between the PI and TPS profiles using a 3% dose difference and 3 mm distance-to-agreement criterion. The mean percentage of pixels with a γ-evaluation value of less than unity was $\overline{P_{\gamma<1}}$ = 95.5% (standard deviation of the pass-rates $\sigma_{P_{\gamma<1}}$ = 8.4%).[2]

Figure 5.8 shows two back-projected dose planes for subjects vP1 and vP2 generated by the VMAT dosimetry technique. Note that many of the doses greatly exceed the prescription dose of 200 cGy (by more than 50%). These doses do not fall along

---

[2] The lower limit of the 95% prediction interval in this case is $P_{\gamma<1}$ = 79.0%

the EPID v-axis (shown with a white line) and therefore they do not represent a physical dose in the patient volume. In Figure 5.9, one-dimensional dose profiles corresponding to the white lines of the dose planes in Figure 5.8 are shown for subjects vP1 and vP2.

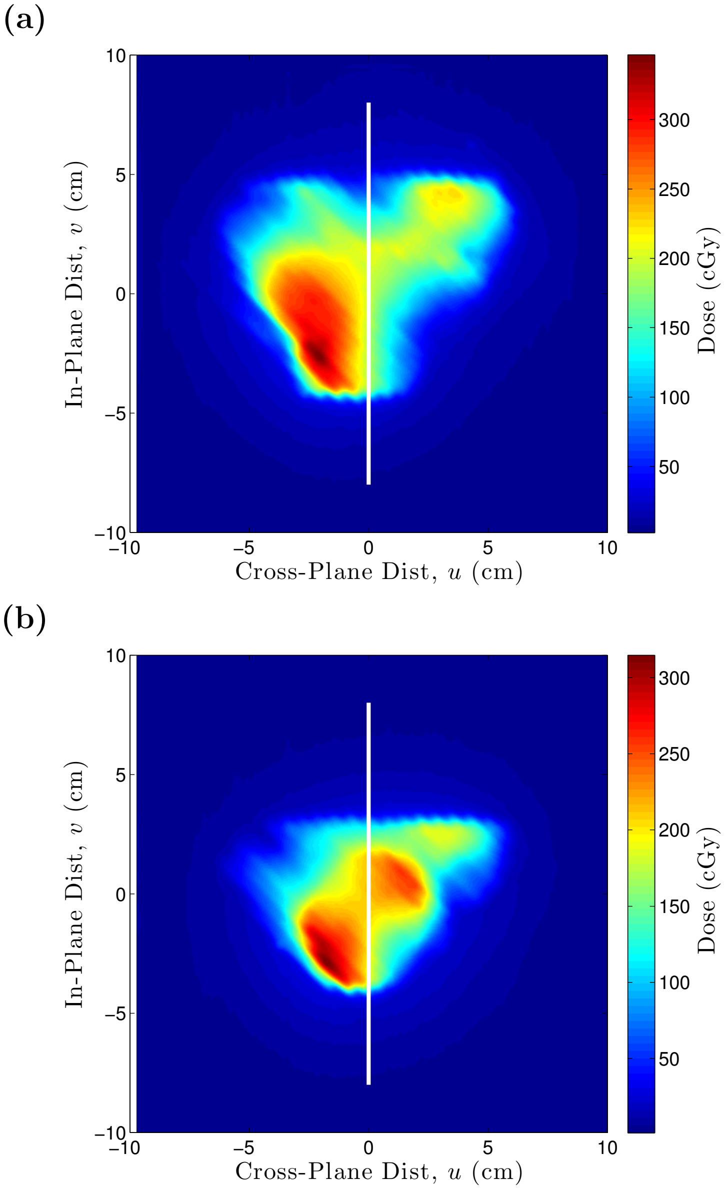

Figure 5.8: Back-projected dose planes for two VMAT prostate cancer treatments showing one fraction from **(a)** Plan vP1 and **(b)** Plan vP2. The location of the profiles plotted in Figure 5.9 are shown with a white line; this profile is the only *in vivo* patient dose.

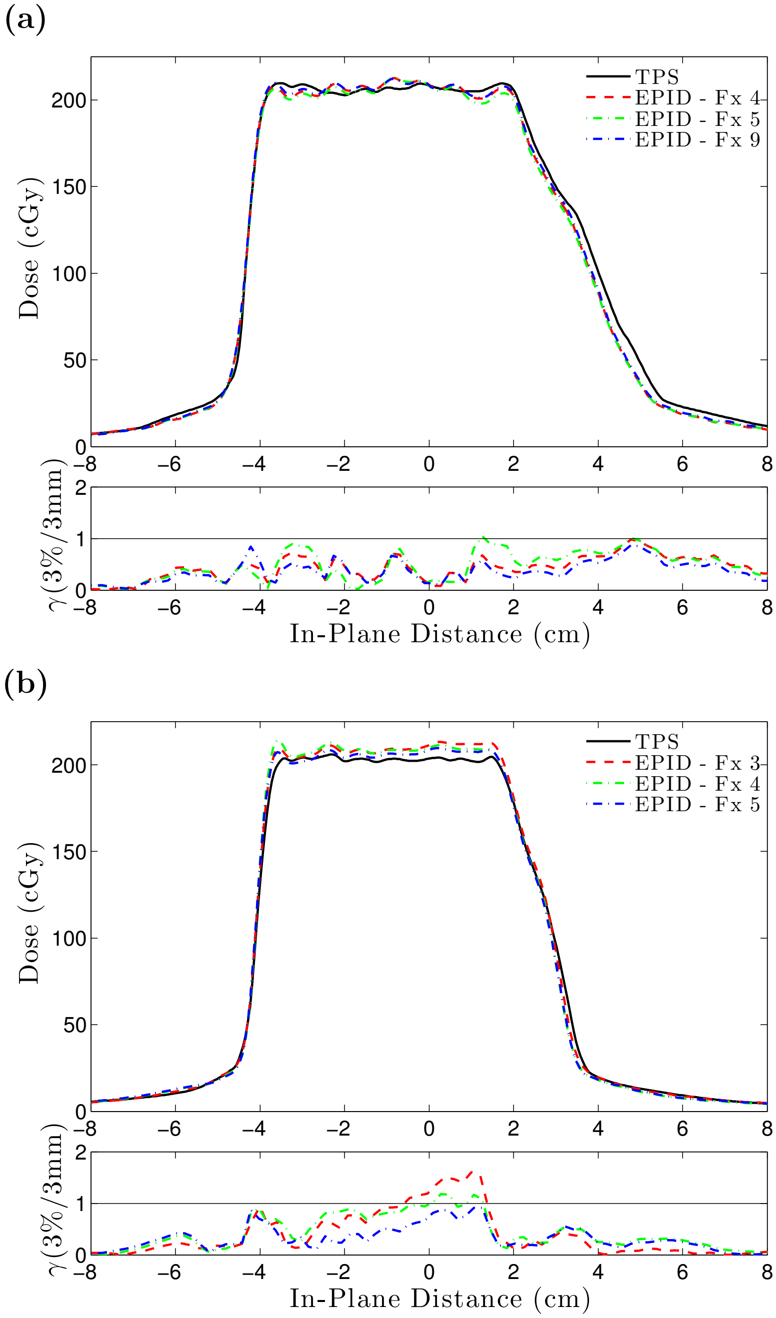

Figure 5.9: Treatment planning system and back-projected dose profiles along the axis of gantry rotation shown for two prostate cancer treatments (top panels), showing **(a)** Plan vP1 and **(b)** Plan vP2. A one-dimensional γ-evaluation is also shown (bottom panel). The inferior direction is towards the negative $x-$axis; the superior direction is towards the positive $x-$axis

Chapter 6

Discussion

In this chapter, a discussion of the two transit EPID dosimetry techniques (IMRT, Section 6.1 and VMAT, Section 6.2) is presented. The accuracy and precision of the EPID dose back-projection techniques are discussed, and references are made to literature values of comparable *in vivo* dosimetry studies where possible.

The portal image-derived back-projected dose distributions generated in this study were generally shown to be consistent with the doses that were calculated by the treatment planning system (TPS). Consistency was determined using three metrics: (i) the isocenter point dose difference (ii) the mean dose difference across the dose profile (VMAT) or plane (IMRT) and (iii) the percentage of pixels passing a γ-evaluation (3%/3mm criteria). Analyzing these three metrics together allowed for a general comparison of the performance of the back-projected dose against the reference dose as calculated by the TPS.

Patient-specific inconsistencies observed in clinical data (deviations between measured and reference dose distributions were likely due to patient-specific uncertainties) as well as general algorithm strengths and deficiencies are addressed in this chapter.

6.1 Clinical IMRT *in vivo* dosimetry

The purpose of validating the EPID back-projection technique on an anthropomorphic phantom was to obtain a baseline of expected range of measurement values for the *in vivo* back-projection algorithm. The anthropomorphic phantom measurements represented the next step in the evolution of the model validation following the calibration conditions of homogeneous water phantoms. Clinical uncertainties - namely, the patient-specific uncertainties that were described in Section 1.2 (e.g. unplanned gas pockets, motion) - are not a factor in phantom measurements.

The purpose of the patient study was to examine the performance of the dose back-projection algorithm under routine clinical conditions, which includes the presence of patient-specific uncertainties.

6.1.1 Accuracy and precision

The IMRT *in vivo* clinical data presented in Section 5.1 were consistent with the phantom measurements that are summarized in Table A.1.

Table 6.1: Comparison of phantom study and clinical results for the IMRT *in vivo* back-projection model.

	Phantom Study	Clinical Study
Isocenter Point Dose Difference ($\delta_{PI} \pm \sigma_{\delta_{PI}}$)	0.1 ± 3.5%	0.0 ± 4.3%
2D Mean Dose Difference ($\Delta_{PI} \pm \sigma_{\Delta_{PI}}$)	1.0 ± 1.7%	-0.2 ± 2.0%
$\gamma-$Evaluation Pass-Rate ($P_{\gamma<1} \pm \sigma_{P_{\gamma<1}}$)	89.7 ± 5.7%	89.6 ± 8.6%

In the three tests (isocenter point dose, planar dose difference and γ-evaluation pass-rates) shown in Table 6.1, the mean values of the two types of measurements (phantom and clinical) were in good agreement. The mean dose difference, Δ_{PI} was approximately one percentage point greater for the phantom measurements compared to the clinical measurements but the two measurements still agreed within one standard deviation. It can be observed that in the case of the clinical study the standard deviations of all the quantities were greater for the clinical study compared to the phantom study. The greater variability of the clinical measurements can primarily be attributed to patient-specific uncertainties. Examples of patient specific uncertainties that were observed are discussed in Section 6.1.2.

Isocenter dose

Table 6.2 presents the results of reconstructed point isocenter dose measurements compared to planning isocenter dose values made by a number of published *in vivo* EPID dosimetry studies. If the isocenter dose comparison of a study was reported as a ratio of portal image dose to TPS dose, the ratio was converted to isocenter dose difference for consistency. The studies presented in the table are broken down by treatment technique. This is not an exhaustive list of all portal image dosimetry studies; however, it is a good representative sample.

The isocenter dose difference of the patient IMRT study presented in Chapter 5 was $\overline{\delta_{PI}} = 0.0 \pm 4.3\%$ (Mean ± 1 SD, $n = 27$ fractions). The definition of the isocenter dose difference is shown in Eq. 5.1. The standard deviation was observed to be slightly greater in this work's IMRT *in vivo* clinical study than in similar studies. It should be noted that three of the four outlying isocenter point dose differences (as shown in Figure 5.4) were due to the three imaging fractions of subject H2. These three outlying isocenter doses are discussed in the context of patient-specific discrepancies in Section 6.1.2.

While the isocenter dose is simple to obtain in the reconstruction geometry of this study, future modifications to the algorithm might allow for the reconstruction dose planes to intersect at the dose reference point (D_{ref}). D_{ref} is necessarily in a region of high dose and low dose gradient and therefore does not suffer from inaccuracies that arise from sharp gradients that might occur near the isocenter dose. This modification may decrease the variance of isocenter point dose data.

Planar dose

For the clinical IMRT *in vivo* dosimetry technique, the planar dose difference was $\overline{\Delta_{PI}} = -0.2 \pm 2.0\%$ (Mean ± 1 SD, $n = 159$ fields) and the $\gamma-$evaluation pass rate was $\overline{P_{\gamma<1}} = 89.6 \pm 8.6\%$ (Mean ± 1 SD, $n = 159$ fields). These measurements were similar to results reported by other planar EPID dosimetry studies (e.g. [13]). The $\gamma-$evaluation values, however, are inherently difficult to compare quantitatively to literature values. The dimensionality (2D vs 3D), dose threshold, detector resolution, dose-difference and distance-to-agreement criteria are all factors when assessing dose distributions and are subject to variability between groups.

By performing a planar dose difference calculation and $\gamma-$evaluation on each dose plane individually, the plan can be analyzed on a field-by-field basis. Unlike the dose to isocenter, which was a composite dose distribution evaluation metric, the planar

Table 6.2: Isocenter point dose measurements, as reported by EPID *in vivo* dosimetry studies. The isocenter dose differences calculated in this study are included for comparison in bold.

Reference	Technique	Reported Iso. Dose Diff. ($\overline{\delta_{PI}} \pm \sigma_{\delta_{PI}}$)	Patient Sample Size
Piermattei et al. (2006) [70]	3DCRT	-1.0 ± 2.5%	40
Francois et al. (2011) [a] [71]	3DCRT	0.2 ± 3.5%	18
Francois et al. (2011) [b] [71]	3DCRT	-1.6 ± 2.4%	20
McDermott et al. (2007) [53]	IMRT	-1.0 ± 1.0%	75
Pecharroman-Gallego et al. (2011)[c] [55]	IMRT	2.6 ± 3.1%	47
Pecharroman-Gallego et al. (2011)[d] [55]	IMRT	0.2 ± 2.0%	47
Wendling et al. (2012) [54]	IMRT	-0.8 ± 1.1%	5
Present Work	**IMRT**	**0.0 ± 4.3%**	**9**
Piermattei et al. (2009) [58]	DCAT[e]	0.1 ± 2.5%	1
Mans et al. (2010) [24]	VMAT	-1.2 ± 0.6%	2
Slosarek et al. (2010) [56]	VMAT	1.7 ± 1.7%	5
Wendling et al. (2012) [54]	VMAT	0.5 ± 1.4%	5
Present Work	**VMAT**	**1.1 ± 1.7%**	**3**

[a] Preliminary feasibility study
[b] Clinical implementation
[c] Calculated patient transmission
[d] Measured patient transmission
[e] Dynamic Conformal Arc Therapy

dose difference and the $\gamma-$evaluation provide a measure of the accuracy delivery of each individual radiation beam.

6.1.2 Patient-specific discrepancies

Subject H2 - Isocenter dose discrepancy

The raw portal images of the subject showing the largest isocenter dose differences (subject H2, where $\delta_{PI} = 15.7\%$, $\delta_{PI} = 6.3\%$, and $\delta_{PI} = 8.6\%$ for fractions one through three respectively) were examined to determine the source of the large discrepancy. Within each fraction, the isocenter dose from the heavily weighted beam at gantry angle 70° was shown to differ nearly 28% from the planned value. Figure 6.1 shows the entrance of this GA 70° beam on the patient. The beam enters through the left side of the neck and exits through the right shoulder.

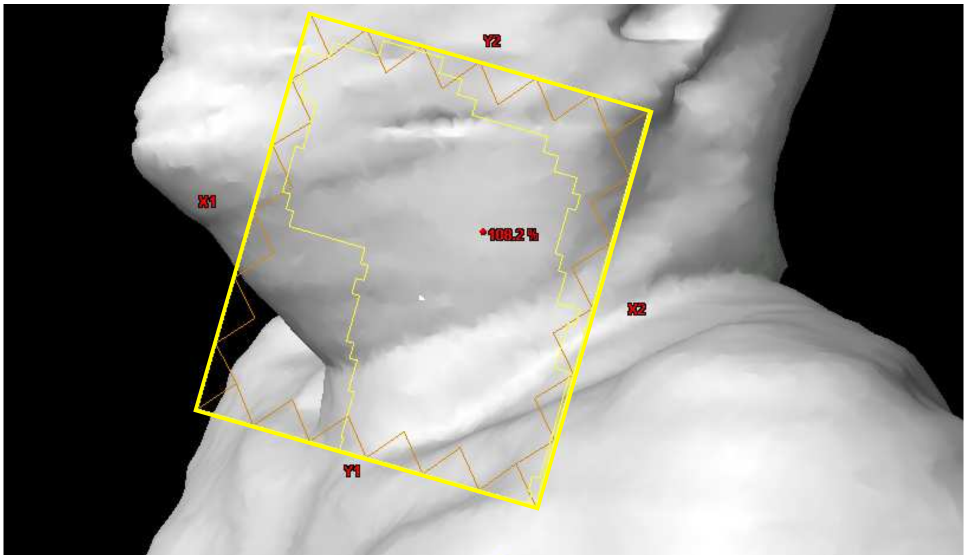

Figure 6.1: Placement of the GA 70° beam on subject H2.

In Figure 6.2, two raw portal images of the beam following transmission through the subject are shown. The isocenter point dose differences of this beam were $\delta_{PI}^{70^\circ} = 27.5\%$ and $\delta_{PI}^{70^\circ} = 11.4\%$, for fractions one and two respectively. Examining Figure 6.2 closely, a larger region of heightened intensity is observed surrounding the isocenter (which is denoted by a blue cross) at fraction one. The high intensity region is decreased in size and the isocenter is in a steep dose gradient at fraction two. Referring again to Figure 6.1, it can be noted that this region of increased intensity occurs at the boundary of the right shoulder blade. Since the shoulder blade was positioned inferiorly compared to its planned position, an apparent dose discrepancy is observed. It should be noted that this discrepancy is likely not clinically relevant in this instance; however, if the beam were to enter from the opposite direction (gantry angle 250°), the isocenter dose would be clinically affected. This patient-specific discrepancy serves to emphasize a key note about EPID dosimetry: any factors in the path of the beam that are unaccounted for (or different from the reference geometry) have the potential to make large dosimetric impacts in the reconstruction model.

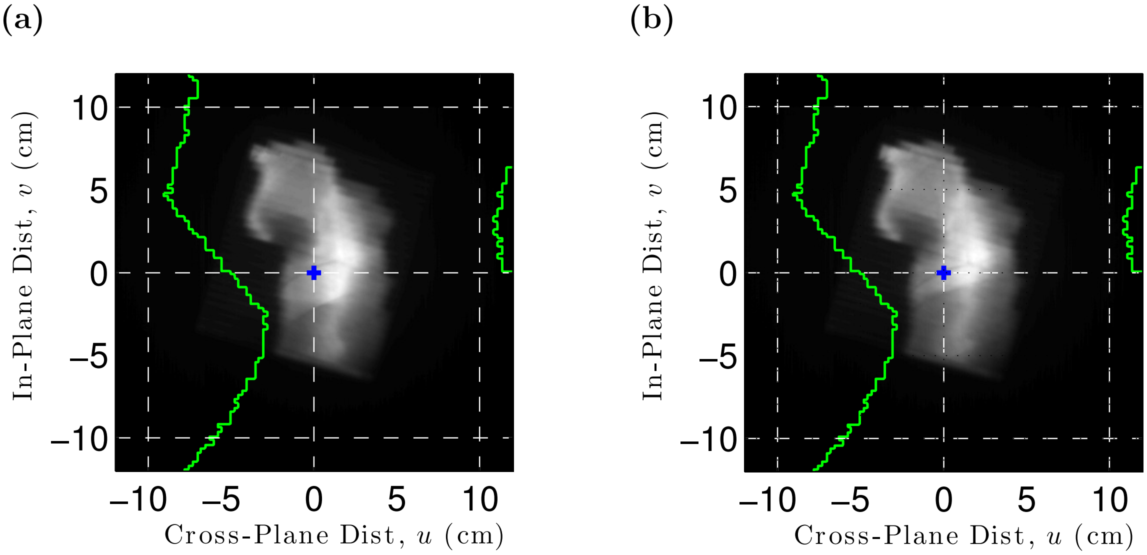

Figure 6.2: Subject H2 raw portal images (edge-enhanced) from two fractions. A positional misalignment was expressed as an isocenter dose difference of **(a)** 27.5% for fraction one compared to an isocenter dose difference of **(b)** 11.4% for fraction two. The subject's body contour is shown in green; the isocenter is denoted by the blue cross.

With the removal of this patient case, the mean isocenter dose difference of the IMRT study shifts from $\overline{\delta_{PI}} = 0.0 \pm 4.3\%$ to $\overline{\delta_{PI}} = -1.2 \pm 2.2\%$. While the mean isocenter dose difference moves slightly away from zero, it still well remains within previous literature values and the standard deviation is reduced by almost one half.

Subject P1 - Planar dose discrepancy

In Figure 5.7, it can be noted that for the IMRT *in vivo* dosimetry study there are four treatment fields with $\gamma-$evaluation pass-rates of less than 60%. These numbers were concerning from an algorithm development standpoint and a dosimetry standpoint.

Investigation of the clinical study results showed that all four of these fields were recorded from subject P1 in fractions three and four.

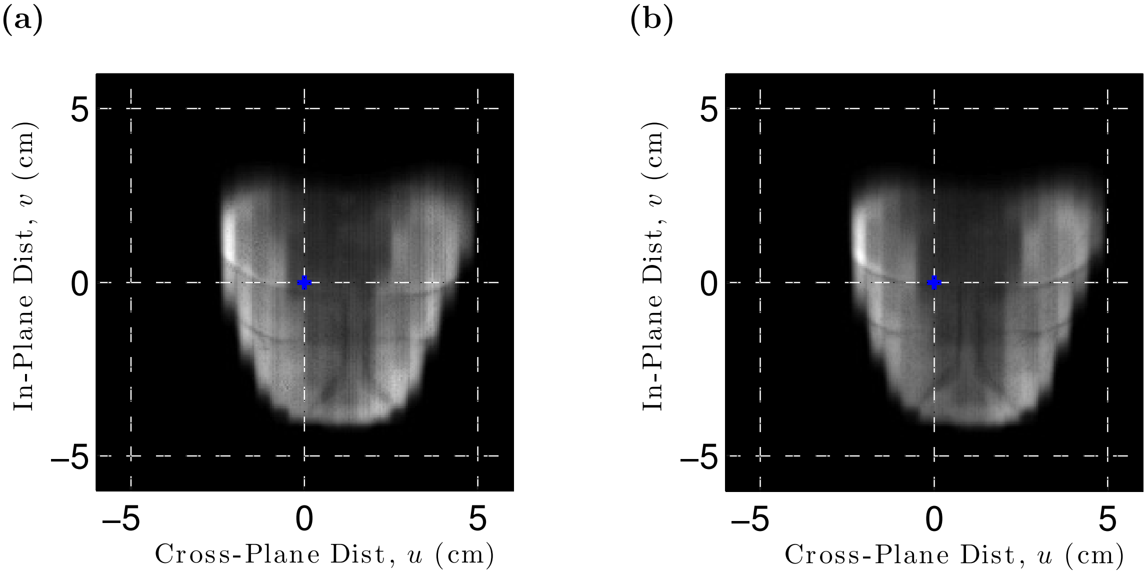

Figure 6.3: Subject P1 raw portal images (edge-enhanced) from two fractions. A positional misalignment was expressed as an $\gamma-$evaluation pass-rate **(a)** 58% for fraction three compared to a pass-rate of **(b)** 97.8% for fraction 34.

Figure 6.3 shows the gantry angle zero (anterior-posterior) beam raw portal image for two fractions for subject P1, one in which the $\gamma-$evaluation pass rate was below 60% and one in which it was above 90%. A comparison of the third fraction's portal image to the digitally reconstructed radiograph (DRR) showed that the patient had shifted by up to 0.6 cm in the left-right direction based on the position of the pubic symphysis. The prostate treatment set-up tolerance is historically ±5 mm at the BCCA - VIC. The shift was sufficient to significantly alter the alignment between treatment and reconstruction geometries so as to create a large comparison error.

Previous phantom studies have examined the relationship between γ-evaluation pass-rates and positional shifts for *in vivo* EPID dosimetry and concluded that alerts were only raised if the shift was greater than one centimeter [54]; therefore, it is possible that additional patient-specific uncertainties may have been at play in this case.

This case highlights the possible magnitude of intra-fractional motion and how, despite daily kV orthogonal alignment to bony anatomy, significant soft tissue shifts can still occur from the planned position during treatment. It should be emphasized that in vivo dosimetry is not a substitute for proper patient positioning or immobilization, but it may have the potential to detect positional errors during treatment.

For evaluating the accuracy of the IMRT *in vivo* dose calculation algorithm, if these four treatment fields are excluded from the pass-rate analysis, the $\gamma-$evaluation pass rate improves to from $\overline{P_{\gamma<1}} = 89.6 \pm 8.6\%$ to $\overline{P_{\gamma<1}} = 90.4 \pm 6.7\%$ (Mean ± 1 SD). Excluding these measurements decreases the standard deviation of the pass-rate distribution by almost two percentage points and brings it closer to that obtained for the phantom measurements.

6.1.3 Algorithm strengths and deficiencies

The reconstructed dose distributions that were generated allowed for an independent verification of the dose delivered for each fraction. In the *in vivo* dose verification models, the patient planning CT set was used to determine several reconstruction parameters (e.g. patient attenuation/transmission, scatter kernel parameters). The back-projection model reconstructs the treated dose in the same geometry that the treatment was planned. It has been proposed that cone beam CT (CBCT) scans might be acquired in advance of each fraction [24]. Reconstruction would therefore occur within the CBCT image set to obtain a more accurate *in vivo* dose at the time of treatment. While CBCT scans would allow for the correction of systematic patient changes during a course treatment (e.g. weight loss) or differences between the planning patient setup and the treated patient setup, this method would still not take into account intra-fraction motion. Furthermore, CBCT scanners suffer from inaccurate CT number calibrations, field-of-view constraints, and the dose from high-quality daily kV CBCT acquisition is not negligible.

Without regular CBCT imaging, is not clear how differences between planning and treatment geometries may translate to differences in the reconstructed dose. It was not within the scope of this study to address systematic patient- or machine-specific uncertainties (e.g. systematic positional offsets, constant dose offsets). However, two examples of patient-specific discrepancies that were discovered are discussed in Section 6.1.2 helped elucidate the effect of positional movement on reconstruction accuracy.

Discrepancies between TPS dose planes and EPID back-projected dose planes are present as the two are calculated using different levels of model sophistication. Since the calculation of the back-projection model kernels were performed using data from homogeneous water phantoms, inhomogeneties are only accounted for by the radiological thickness and depth electron density scaling procedure. Lateral scaling of scatter kernels, as performed in AAA, is not implemented in the EPID dose back-projection model. The reconstruction assumes that the plane of reconstruction is surrounded by an infinite water medium; therefore, edge-effects are apparent in some reconstructed dose planes - particularly at sharp boundaries.

The back-projection algorithm is fast, even when running uncompiled MATLAB research code. The computational time, using an Intel Core 2 Duo CPU (1.97 GHz, 2 GB RAM) at the BCCA-VIC, for the first fraction of a five-field prostate plan was approximately 130 seconds. The computational time for the first fraction of a seven-field head and neck plan on the same machine was approximately 160 seconds. Recalculating the EPID back-projected dose for subsequent fractions took approximately 45 seconds and 65 seconds for the prostate and head and neck plans respectively. The computational time was decreased for subsequent fractions since the patient transmission factors needed only to be calculated at the first fraction.

6.2 Clinical VMAT *in vivo* dosimetry

6.2.1 Accuracy and precision

The VMAT *in vivo* clinical data presented in Section 5.2 were consistent with the phantom measurements that are summarized in Table A.2.

Table 6.3: Comparison of phantom study and clinical results for the VMAT *in vivo* back-projection model.

	Phantom Study	Clinical Study
Isocenter Point Dose Difference ($\delta_{PI} \pm \sigma_{\delta_{PI}}$)	4.1 ± 2.9%	1.1 ± 1.7%
2D Mean Dose Difference ($\Delta_{PI} \pm \sigma_{\Delta_{PI}}$)	1.0 ± 1.1%	0.0 ± 1.3%
$\gamma-$Evaluation Pass-Rate ($P_{\gamma<1} \pm \sigma_{P_{\gamma<1}}$)	90.1 ± 9.5%	95.5 ± 8.4%

The mean values of the phantom and clinical measurements were in good agreement as shown in Table 6.3; however, there were some notable exceptions. The mean isocenter dose difference of the phantom measurements was three percentage points greater than the mean isocenter dose difference of the clinical measurements. Phantom prostate treatment plans were chosen to have dual arcs as the BCCA-VIC VMAT prostate planning method had not yet been determined. In the case of dual arcs, the two dose profiles along the gantry rotation axis had a greater variation within the field compared to single arc plans where the dose along the gantry rotation axis was relatively constant at the prescription dose. Therefore, when convolved with a patient scatter kernel, such as the one used in this study, the dose in the "valley" region of the distributions may have been overestimated.

Isocenter dose

The isocenter dose difference of the patient VMAT study was $\overline{\delta_{PI}} = 1.1 \pm 1.7\%$ (Mean ± 1 SD, $n = 9$ fractions). The mean and standard deviation of the isocenter dose difference were comparable to previous VMAT EPID dosimetry studies, as shown in Table 6.2. The isocenter dose differences from single integrated portal images were generally consistent with VMAT cine-mode EPID dosimetry studies, despite having previously been described as "inappropriate" for VMAT verification [24].

In many VMAT treatments, the isocenter is frequently chosen to be in the planning treatment volume (PTV) and therefore the dose to isocenter alone is a clinically meaningful measurement. However, it should be noted that the isocenter may be located outside of the PTV, for example in the case of multiple PTVs (e.g. primary and nodal PTVs).

Profile evaluation

The mean profile $\gamma-$evaluation pass-rate of the VMAT study was $\overline{P_{\gamma<1}} = 95.5 \pm 8.4\%$ (Mean ± 1 SD, $n = 9$ fields). and the mean profile dose difference was $\overline{\Delta_{PI}} = 0.0 \pm 1.3\%$ (Mean ± 1 SD, $n = 9$ fields).

The low profile dose difference and high $\gamma-$evaluation pass-rates of the measured dose to the gantry rotation axis show that this *in vivo* EPID dosimetry technique for VMAT treatments is effective, and meaningful dose information is contained throughout the EPID $v-$axis signal. This signal can be used to accurately calculate the dose to the gantry rotation axis *in vivo*.

6.2.2 Patient-specific discrepancies

In part due to the limited sample size of the VMAT patient study, few patient-specific discrepancies were observed. The variability of point and profile evaluation metrics was minimal within each subject's data set, with the slight exception of the third fraction of subject vP2's treatment shown in Figure 5.9(b). The subject's CBCT scan acquired before this fraction did not show the presence of rectal gas filling or any other significant discrepancies which might significantly change the patient's anatomy compared to the conditions of the planning CT. Unlike for static gantry angles (IMRT), the VMAT single integrated portal images were inconclusive as to whether any intrafraction motion occurred.

6.2.3 Algorithm strengths and deficiencies

The VMAT *in vivo* dose reconstruction algorithm detailed in this thesis suffers from the same systematic discrepancies as the IMRT back-projection algorithm. The two techniques share the same model and associated parameters, except in VMAT model the dose reconstruction occurs in a rotationally averaged virtual representation of the patient rather than the patient's CT image set. The rotational averaging relies on knowledge of the meterset weight (MW) distribution of the arcs. In this sense, the dose verification in this model is not wholly independent of the treatment planning system. However, it not unreasonable to have a knowledge of the beam weighting since the purpose of the EPID back-projection is to detect differences from the planned dose. Differences between back-projected and planned doses could be substantial if the irradiated anatomy or meterset weights were significantly different than planned throughout the arc.

An additional uncertainty associated with the VMAT dose reconstruction technique is encountered when selecting the appropriate profile on the back-projected EPID dose for comparison to the TPS dose. There is an uncertainty associated with the EPID positional set-up and gravitational sag of the device. Thus, the algorithm searches EPID pixel columns within a neighbourhood of ±3mm from the nominal EPID $v-$axis. The EPID dose profile that agrees most closely with the planned dose along the axis of gantry rotation, as determined by the amount of pixels passing a one-dimensional 3%/3mm $\gamma-$evaluation, is selected and displayed. This profile search is one method of taking into account dose gradients in the cross-plane direction that would otherwise be overlooked by a one-dimensional γ-evaluation.

The VMAT back-projection reconstruction is limited to the dose along the gantry rotation axis. By limiting the reconstruction and comparison to this profile, much of the dose in the cross-plane direction of the EPID is lost. However, the signal off axis from the EPID $v-$axis does not share a one-to-one correspondence with an *in vivo* patient dose and is therefore not appropriate to use for a patient dose calculation.

The computational time for the first fraction of a single arc clinical prostate plan was approximately 45 seconds. Recalculating the EPID back-projected dose required approximately five seconds for subsequent fractions.

Chapter 7

Conclusions

In this thesis, a technique for portal image-based *in vivo* IMRT treatment verification was developed and validated. First, a portal image dose plane was calculated following transmission through the patient using an integrated portal image. This portal image dose plane was calculated by applying a pixel value-to-dose calibration, deconvolving the lateral scatter within the EPID, applying empirical dosimetric corrections, and accounting for beam hardening. The patient-to-EPID scattered radiation was deconvolved using a simple model of the scattering process in order to generate the portal image dose plane due to primary radiation. The primary dose plane was back-projected through a model of the patient and convolved with a kernel that represented scattering radiation within the patient to reconstruct the *in vivo* dose.

The modelling technique and parameters were presented, and initial characterizations of the IMRT dose reconstruction model on phantom and human subjects were reported.

The feasibility of a dose back-projection technique for VMAT treatments using single integrated portal images was developed by adapting the IMRT dose back-projection model. The VMAT *in vivo* dosimetry formalism required that single integrated portal images were acquired for each arc. These images were used to calculate the dose along the gantry rotation axis. The modifications of the IMRT technique for VMAT treatment verification (primarily, the use of a rotationally averaged patient representation) were discussed. Initial characterizations of the VMAT dose reconstruction model on phantom and human subjects were also reported.

The EPID dose back-projection techniques evolved from calibration and reconstruction in CT sets of homogenous phantoms, anthropomorphic phantoms, and finally human subjects. A preliminary institutional study showed that the techniques developed were suitable and clinically realizable.

The accuracy and precision of the IMRT and VMAT dose back-projection techniques outlined in this thesis were shown to be strong. Isocenter point dose measurements, planar (IMRT) or profile (VMAT) mean dose differences, and $\gamma-$evaluations were in good agreement. Where large discrepancies between reconstructed and reference doses were noted, possible sources of the discrepancies were identified.

The total time time commitment required for a single fraction verification, from file export to calculation, is on the order of approximately ten minutes for the first fraction. The only clinical restriction at the time of treatment is that the Varian TrueBeam linear accelerator does not permit the field delivery to be sequenced automatically when portal images are acquired, extending treatment time by approximately 30-60 seconds. The patient's DICOM plan file, structure set, field dose files, and planning CT set must be exported manually from the treatment planning system. The treatment session portal images must also be manually selected and exported from the server. The program is then run for the first time, with the user required to input several factors (e.g. couch thickness), thereby generating the necessary reconstruction parameters and performing the dose reconstruction for the first fraction. Each subsequent fraction takes approximately five minutes for manual image export and reconstruction. For reference, a complete set of one-time pre-treatment patient specific QA can take between one to two hours to complete. It was not within the scope of this thesis to determine whether or not this *in vivo* EPID dosimetry technique is appropriate for regular clinical use; however, the commitment required to do so has been outlined.

Since the time commitment of EPID dosimetry is much less than pre-treatment dosimetry, if the first several fractions were solely verified *in vivo*, a large amount of time and resources could be saved [53]. However, if pre-treatment verification were to be replaced or supplemented with *in vivo* dosimetry, confidence and action levels must first be developed on a larger patient sample. A clinical protocol for *in vivo* EPID dosimetry would also be required, detailing the circumstances and frequency of *in vivo* EPID dosimetry should it be incorporated into a clinical routine.

The EPID *in vivo* dosimetry techniques presented in this thesis build on over seven years of portal image-based IMRT pre-treatment verification the BCCA-VIC [14] and is the first implementation of transit EPID dosimetry at this institution. It is concluded that EPID dosimetry is feasible for *in vivo* treatment verification at the the BCCA - VIC if and when an appropriate implementation scheme is adopted.

Bibliography

[1] BC Cancer Agency. Radiation therapy. http://www.bccancer.bc.ca/ PPI/ CancerTreatment/ RadiationTherapy/ default.htm, July 2011.

[2] M. K. Kam, R. Chau, J. Suen, P. H. Choi, and P. M. Teo. Intensity-modulated radiotherapy in nasopharyngeal carcinoma: Dosimetric advantage over conventional plans and feasibility of dose escalation. *Int. J. Radiat. Oncol.*, 56(1): 145–157, 2003.

[3] I. S. Grills, D. Yan, A. A. Martinez, F. A. Vicini, J. W. Wong, and L. L. Kestin. Potential for reduced toxicity and dose escalation in the treatment of inoperable non small-cell lung cancer: A comparison of intensity-modulated radiation therapy (IMRT), 3D conformal radiation, and elective nodal irradiation. *Int. J. Radiat. Oncol.*, 57(3):875–890, 2003.

[4] D. L. W. Kwong, J. S. T. Sham, L. H. T. Leung, A. C. K. Cheng, W. M. Ng, P. W. K. Kwong, W. M. Lui, C. C. Yau, P. M. Wu, W. Wei, and G. Au. Preliminary results of radiation dose escalation for locally advanced nasopharyngeal carcinoma. *Int. J. Radiat. Oncol.*, 64(1):374–381, 2006.

[5] K. Otto. Volumetric modulated arc therapy: IMRT in a single gantry arc. *Med. Phys.*, 35(1):310–318, 2008.

[6] C. C. Popescu, I. A. Olivotto, W. A. Beckham, W. Ansbacher, S. Zavgorodni, R. Shaffer, E. S. Wai, and K. Otto. Volumetric modulated arc therapy improves dosimetry and reduces treatment time compared to conventional intensity-modulated radiotherapy for locoregional radiotherapy of left-sided breast cancer and internal mammary nodes. *Int. J. Radiat. Oncol.*, 76(1):287–295, 2010.

[7] D. Palma, E. Vollans, K. James, S. Nakano, V. Moiseenko, R. Shaffer, M. McKenzie, J. Morris, and K. Otto. Volumetric modulated arc therapy for delivery of prostate radiotherapy: Comparison with intensity modulated radiotherapy and

three-dimensional conformal radiotherapy. *Int. J. Radiat. Oncol.*, 72(4):996–1001, 2008.

[8] R. W. Kopp, M. Duff, F. Catalfamo, D. Shah, M. Rajecki, and K. Ahmad. VMAT vs. 7-field-IMRT: Assessing the dosimetric parameters of prostate cancer treatment with a 292-patient sample. *Med. Dosim.*, 36(4):365–372, 2011.

[9] M. C. Kirkby and A. G. Glendinning. Developments in electronic portal imaging systems. *Brit. J. Radiol.*, 79:S50–S65, 2006.

[10] T. Bortfield, R. Schmidt-Ullrich, W. De Neve, and D. E. Wazer. *Image Guided IMRT*. Springer-Verlag, Berlin, 2006.

[11] P. T. Truong, E. Berthelet, V. Patenaude, J. Bishop, B. Sandwith, V. Moravan, W. Beckham, T. Mitchell, and I. A. Olivotto. Setup variations in locoregional radiotherapy for breast cancer: An electronic portal imaging study. *Brit. J. Radiol.*, 78:742–745, 2005.

[12] P. Greer and C. C. Popescu. Dosimetric properties of an amorphous silicon electronic portal imaging device for verification of dynamic intensity modulated radiation therapy. *Med. Phys.*, 30(7):1618–1627, 2003.

[13] W. van Elmpt, L. N. McDermott, S. Nijsten, M. Wendling, P. Lambin, and B. J. Mijnheer. A literature review of electronic portal imaging for radiotherapy dosimetry. *Radiother. Oncol.*, 88:289–309, 2008.

[14] W. Ansbacher. Three-dimensional portal image-based dose reconstruction in a virtual phantom for rapid evaluation of IMRT plans. *Med. Phys.*, 33(9):3369–3382, 2006.

[15] W. Ansbacher, C. L. Swift, and P. B. Greer. An evaluation of cine-mode 3D portal image dosimetry for volumetric modulated arc therapy. *J. Phys. Conf. Ser.*, 250:012022, 2010.

[16] W. Bogdanich. Radiation Offers New Cures, and Ways to Do Harm. http://www.nytimes.com/2010/01/24/health/24radiation.html?pagewanted=all&_r=0, 24 Jan 2010 2010.

[17] French doctors and radiologist jailed for radiation overdoses. http://www.telegraph.co.uk/news/worldnews/europe/france/9837803/French-doctors-and-radiologist-jailed-for-radiation-overdoses.html, 30 Jan 2013 2013.

[18] Institut National du Cancer (INCa). Guide pour la practique quotidienne de la dosimetrie *in vivo* en radiotherapie externe, 2008.

[19] Swedish Radiation Protection Institute. The Swedish Radiation Protection Institute's Regulations on Radiation Therapy (SSI FS 2000:4), 2000.

[20] B. J. Mijnheer and D. Georg. *Guidelines for verification of IMRT, ESTRO Booklet No. 9*. ESTRO, Brussels, 1st edition, 2008.

[21] J. L. Leman. *In vivo* dosimetry; essential or unnecessary? *J. Radiother. Pract.*, 11:55–61, 2012.

[22] V. N. Hansen, P. M. Evans, and W. Swindell. The application of transit dosimetry to precision radiotherapy. *Med. Phys.*, 23(5):713–721, 1996.

[23] M. Wendling, R. J. W. Louwe, L. N. McDermott, J. J. Sonke, M. van Herk, and B. J. Mijnheer. Accurate two-dimensional IMRT verification using a back-projection EPID dosimetry method. *Med. Phys.*, 33(2):259–273, 2006.

[24] A. Mans, P. Remeijer, I. Olaciregui-Ruiz, M. Wendling, J. J. Sonke, B. J. Mijnheer, M. van Herk, and J. C. Stroom. 3D Dosimetric verification of volumetric-modulated arc therapy by portal dosimetry. *Radiother. Oncol.*, 94:181–187, 2010.

[25] E. Podgorsak. *Review of Radiation Oncology Physics: A Handbook for Teachers and Students*. International Atomic Energy Agency, Vienna, AT, 2005.

[26] M. G. Herman, J. M. Balter, D. A. Jaffray, K. P. McGee, P. Munro, S. Shalev, M. van Herk, and J. W. Wong. Clinical use of electronic portal imaging: Report of AAPM Radiation Therapy Committee Task Group 58. *Med. Phys.*, 28(5): 712–737, 2001.

[27] M. van Herk. Physical aspects of a liquid-filled ionization chamber with pulsed polarizing voltage. *Med. Phys.*, 18(4):692–702, 1991.

[28] H. Meertens, M. van Herk, J. Bijhold, and H. Bartelink. First clinical experience with a newly developed electronic portal imaging device. *Int. J. Radiat. Oncol.*, 18(5):1173–1181, 1990.

[29] V.G. Althof, J.C. de Boer, H. Huizenga, J.C. Stroom, A.G. Visser, and B.N. Swanenburg. Physical characteristics of a commercial electronic portal imaging device. *Med. Phys.*, 23(11):1845–1855, 1996.

[30] L.E. Antonuk, J. Yorkston, W. Huang, J.H. Siewerdsen, J.M. Boudry, Y. el Mohri, and M.V. Marx. A real-time, flat-panel, amorphous silicon, digital x-ray imager. *Radiographics*, 15(4):993–1000, 1995.

[31] J. V. Siebers, J. O. Kim, L. Ko, P. J. Keall, and R. Mohan. Monte Carlo computation of dosimetric amorphous silicon electronic portal images. *Med. Phys.*, 31(7):2135–2146, 2004.

[32] Varian Medical Systems Inc. PortalVision aS1000: The state of the art in electronic portal imaging, 2006.

[33] P. Rowshanfarzad, M. Sabet, D. J. O'Connor, P. M. McCowan, B. M. C. McCurdy, and P. B. Greer. Detection and correction for EPID and gantry sag during arc delivery using cine EPID imaging. *Med. Phys.*, 39(2):623–635, 2012.

[34] S. L. Berry, C. S. Polvorosa, and C. S Wuu. A field size specific backscatter correction algorithm for accurate EPID dosimetry. *Med. Phys.*, 37(6):2425–2434, 2010.

[35] P. Rowshanfarzad, B. M. C. McCurdy, M. Sabet, C. Lee, D. J. O'Connor, and P. B. Greer. Measurement and modeling of the effect of support arm backscatter on dosimetry with a Varian EPID. *Med. Phys.*, 37(5):2269–2278, 2010.

[36] Varian Medical Systems Inc. TrueBeam Technical Reference Guide - Volume 2: Imaging (BJ01671R01, Revision D), 2011.

[37] F. H. Attix. *Introduction to Radiological Physics and Radiation Dosimetry.* Wiley-VCH, Germany, 2004.

[38] A. van Esch, T. Depuydt, and P. Huyskens. The use of an aSi-based EPID for routine absolute dosimetric pre-treatment verification of dynamic IMRT fields. *Radiother. Oncol.*, 71:223–234, 2004.

[39] L. N. McDermott, S. Nijsten, J. J. Sonke, M. Partridge, M. van Herk, and B. J. Mijnheer. Comparison of ghosting effects for three commercial a-Si EPIDs. *Med. Phys.*, 33(7):2448–2451, 2006.

[40] A. Ahnesjo, M. Saxner, and A. Trepp. A pencil beam model for photon dose calculation. *Med. Phys.*, 19(2):263–273, 1992.

[41] P. R. M. Storchi, L. J. van Battum, and E. Woudstra. Calculation of a pencil beam kernel from measured photon beam data. *Phys. Med. Biol*, 44:2917–2928, 1999.

[42] A. van Esch, L. Tillikainen, J. Pyykkonen, M. Tenhunen, H. Helminen, S. Siljamaki, J. Alakuijala, M. Paiusco, M. Iori, and D. P. Huyskens. Testing of the analytical anisotropic algorithm for photon dose calculation. *Med. Phys.*, 33(11): 4130–4149, 2006.

[43] A. Fogliata, G. Nicolini, E. Vanetti, A. Clivio, and L. Cozzi. Dosimetric validation of the anisotropic analytical algorithm for photon dose calculation: Fundamental characterization in water. *Phys. Med. Biol*, 51:1421–1438, 2006.

[44] C. M. Bragg and J. Conway. Dosimetric verification of the anisotropic analytical algorithm for radiotherapy treatment planning. *Radiother. Oncol.*, 81(3):315–323, 2006.

[45] D. J. Low, W. B. Harms, S. Mutic, and J. A. Purdy. A technique for the quantitative evaluation of dose distributions. *Med. Phys.*, 25(5):656–661, 1998.

[46] B. E. Nelms and J. A. Simon. A survey on planar IMRT QA analysis. *J. Appl. Clin. Med. Phys.*, 8(3):76–90, 2007.

[47] D. A. Low and J. F. Dempsey. Evaluation of the gamma dose distribution comparison method. *Med. Phys.*, 30(9):2455–2464, 2003.

[48] D. W. Bailey, B. E. Nelms, K. Attwood, L. Kumaraswamy, and M. B. Podgorsak. Statistical variability and confidence intervals for planar dose QA pass rates. *Med. Phys.*, 38(11):6053–6064, 2011.

[49] A. Bakai, M. Alber, and F. Nusslin. A revision of the γ-evaluation concept for the comparison of dose distributions. *Phys. Med. Biol*, 48:3543–3553, 2003.

[50] S. L. Berry, R. D Sheu, C. S. Polvorosa, and C. S Wuu. Implementation of EPID transit dosimetry based on a through-air dosimetry algorithm. *Med. Phys.*, 39 (1):87–98, 2012.

[51] J. Kinsman and P. Humphrey. Portal imaging. *Brit. J. Radiol.*, 78:681–682, 2005.

[52] M. Wendling, L. N. McDermott, A. Mans, J. J. Sonke, M. van Herk, and B. J. Mijnheer. A simple backprojection algorithm for 3D *in vivo* EPID dosimetry of IMRT treatments. *Med. Phys.*, 36(7):3310–3321, 2009.

[53] L. N. McDermott, M. Wendling, J. J. Sonke, M. van Herk, and B. J. Mijnheer. Replacing pretreatment verification with *in vivo* EPID dosimetry for prostate IMRT. *Int. J. Radiat. Oncol.*, 67(5):1568–1577, 2007.

[54] M. Wendling, L. N. McDermott, A. Mans, I. Olaciregui-Ruiz, R. Pecharroman-Gallego, J. J. Sonke, J. C. Stroom, M. van Herk, and B. J. Mijnheer. *In aqua vivo* EPID dosimetry. *Med. Phys.*, 39(1):367–377, 2012.

[55] R. Pecharroman-Gallego, A. Mans, J. J. Sonke, J. C. Stroom, I. Olaciregui-Ruiz, M. van Herk, and B. J. Mijnheer. Simplifying EPID dosimetry for IMRT treatment verification. *Med. Phys.*, 28(2):983–992, 2011.

[56] K. Slorasek, M. Szlag, B. Bekman, and A. Gradziel. EPID *in vivo* dosimetry in RapidArc technique. *Rep. Prac. Oncol. Radiother.*, 15:8–14, 2010.

[57] B. M. C. McCurdy and P. B. Greer. Dosimetric properties of an amorphous-silicon EPID used in continuous acquisition mode for application for application to dynamic and arc IMRT. *Med. Phys.*, 36(7):3028–3039, 2009.

[58] A. Piermattei, A. Fidanzio, L. Azario, F. Greco, A. Mameli, S. Cilla, L. Grimaldi, G. D'Onofrio, B. G. Augelli, G. Stimato, D. Gaudino, S. Ramella, R. D'Angelillo, F. Cellini, and L. Trodella. In patient dose reconstruction using a cine acquisition for dynamic arc radiation therapy. *Med. Biol. Eng. Comput.*, 47:425–433, 2009.

[59] A. Fidanzio, A. Mameli, E. Placidi, F. Greco, G. Stimato, D. Gaudino, S. Ramella, R. D'Angelillo, F. Cellini, L. Trodella, S. Cilla, L. Grimaldi, G. D'Onofrio, L. Azario, and A. Piermattei. EPID cine acquisition mode for *in vivo* dosimetry in dynamic arc radiation therapy. *Nucl. Instrum. Meth. B*, 266:658–666, 2008.

[60] A. Hussain, E. Villarreal-Barajas, D. Brown, and P. Dunscombe. Validation of the eclipse aaa algorithm at extended ssd. *J. Appl. Clin. Med. Phys.*, 11(3): 90–100, 2010.

[61] J. Chen, C. F. Chuang, O. Morin, M. Aubin, and J. Pouliot. Calibration of an amorphous-silicon flat panel portal imager for exit-beam dosimetry. *Med. Phys.*, 33(3):584–594, 2006.

[62] C. Kirkby and R. Sloboda. Comprehensive Monte Carlo calculation of the point spread function for a commercial a-Si EPID. *Med. Phys.*, 32(4):1115–1127, 2005.

[63] C. Kirkby and R. Sloboda. Consequences of the spectral response of an a-Si EPID and implications for dosimetric calibration. *Med. Phys.*, 32(8):2649–2658, 2005.

[64] J.C. Russ. *The Handbook of Image Processing.* CRC Press, Boca Raton, FL, 6th edition, 2011.

[65] L. N. McDermott, R. J. W. Louwe, J. J. Sonke, M. van Herk, and B. J. Mijnheer. Dose-response and ghosting effects of an amorphous silicon electronic portal imaging device. *Med. Phys.*, 31(2):285–295, 2004.

[66] D. A. Jaffray, J. J. Battista, A. Fenster, and P. Munro. X-ray scatter in megavoltage transmission radiography: Physical characteristics and influence on image quality. *Med. Phys.*, 21(1):45–60, 1994.

[67] E. Vanetti de Palma, L. Conte, G. Nicolini, P. Stucchi, C. Mordacchini, E. Cassani, and R. Novario. Experimental method to obtain scattering contribution in portal dose images. *Physica Medica*, 21(1):31–40, 2005.

[68] L. Spies and T. Bortfield. Analytical scatter kernels for portal imaging at 6 MV. *Med. Phys.*, 28(4):553–559, 2001.

[69] R. L. Siddon. Fast calculation of the exact radiological path for a three-dimensional CT array. *Med. Phys.*, 12(2):252–255, 1985.

[70] A. Piermattei, A. Fidanzio, G. Stimato, L. Azario, L. Grimaldi, G. D'Onofrio, S. Cilla, M. Balducci, M. A. Gambacorta, N. Di Napoli, and N. Cellini. *In vivo* dosimetry by an aSi-based EPID. *Med. Phys.*, 33(11):4414–4422, 2006.

[71] P. Francois, P. Boissard, L. Berger, and A. Mazal. *In vivo* dose verification from back projection of a transit dose measurement on the central axis of photon beams. *Phys. Medica*, 27:1–10, 2011.

Appendix A

Additional Information

A.1 Phantom IMRT *in vivo* dosimetry

Seven IMRT treatment plans (39 fields) were exported from archived clinical treatment plans for delivery to an anthropomorphic phantom. The intended treatment site was matched up with the approximate corresponding site on the phantom. The treatments were delivered and integrated portal images were acquired. The images were back-projected using the IMRT *in vivo* dosimetry technique to reconstruct the phantom dose. A summary of these measurements is shown in Table A.1.

Table A.1: Summary of IMRT *in vivo* dosimetry quantities for anthropomorphic phantom measurements.

Site (Fields)	Isocenter Point Difference δ_{PI} (%)	Mean Dose Difference Δ_{PI}, [Min,Max] (%)	Mean $\gamma-$Evaluation Pass Rate $P_{\gamma<1}$, [Min,Max] (%)
Base of Tongue (7)	-1.7	-0.3, [-1.6, 2.1]	86.6, [79.0, 97.4]
Right Parotid (5)	0.6	1.9, [-0.6, 4.8]	87.8, [83.0, 92.0]
Left Neck (7)	-1.1	0.5, [-0.9, 2.1]	88.7, [77.6, 95.8]
Brain (5)	-6.3	-0.7, [-2.2, -0.1]	92.4, [86.7, 100]
Prostate (5)	3.2	1.6, [0.8, 2.5]	91.9, [85.3, 99.0]
Prostate (5)	3.6	2.1, [1.4, 2.5]	90.3, [85.0, 97.5]
Prostate (5)	2.4	2.4, [2.0, 2.9]	91.6, [86.7, 98.0]
Mean ± 1 SD:	0.1% ± 3.5%	1.0% ± 1.7%	89.7% ± 5.7%

A.2 Phantom VMAT *in vivo* dosimetry

Ten RapidArc treatment plans (22 fields) were generated retrospectively on archived clinical data sets. The plans were optimized in order to satisfy plan objectives including planning treatment volume (PTV) coverage and organ-at-risk (OAR) sparing. The plans consisted of either one or two 360° treatment arcs. Once a plan had been generated, the treatment fields were transferred to a CT scan of the anthropomorphic phantom and the dose was recalculated. The treatments were delivered and integrated portal images were acquired. The images were back-projected using the VMAT *in vivo* dosimetry technique to reconstruct the phantom dose at the gantry rotation axis. A summary of the results of the phantom measurements is shown in Table A.2.

Table A.2: Summary of VMAT *in vivo* dosimetry quantities for anthropomorphic phantom measurements.

Site (Arcs)	Isocenter Point Difference δ_{PI} (%)	Mean Profile Difference Δ_{PI} (%)	$\gamma-$Evaluation Pass Rate $P_{\gamma<1}$ (%)
Base of Tongue (1)	9.3[a]	1.1	79.0
Brain (1)	0.9	1.1	97.3
Prostate (2)	4.2	-0.1, 1.5	94.5, 96.0
Prostate (2)	2.2	-0.6, 0.6	93.1, 100
Prostate (2)	4.4	1.2, 1.5	75.8, 99.3
Prostate (2)	7.3	2.0, 3.3	72.8, 79.5
Prostate (2)	2.7	-0.3, 1.7	78.9, 100
Prostate (2)	2.2	-0.1, 0.1	91.5, 99.5
Prostate (2)	1.2	0.7, 1.0	93.3, 99.4
Prostate (2)	7.0	0.9, 3.1	79.9, 95.8
Mean ± 1 SD:	4.1 ± 2.9%	1.0 ± 1.1%	90.1 ± 9.5%

---

[a] In this plan, the isocenter was not in the PTV. This measurement point fell along a steep dose gradient at the boundary of a region of uniform high dose, thus contributing to a large isocenter dose difference.